# Measurements of Sunyaev-Zel'dovich Effect Scaling Relations for Clusters of Galaxies

B.A. Benson[1,2], S.E. Church[2], P.A.R. Ade[3], J.J. Bock[4,5], K.M.Ganga[6], C.N. Henson[2,7], & K.L. Thompson[2]

bbenson@bolo.berkeley.edu

## ABSTRACT

We present new measurements of the Sunyaev-Zel'dovich (SZ) effect from clusters of galaxies using the Sunyaev-Zel'dovich Infrared Experiment (SuZIE II). We combine these new measurements with previous cluster observations with the SuZIE instrument to form a sample of 15 clusters of galaxies. For this sample we calculate the central Comptonization, $y_0$, and the integrated SZ flux decrement, $S$, for each of our clusters. We find that the integrated SZ flux is a more robust observable derived from our measurements than the central Comptonization due to inadequacies in the spatial modelling of the intra-cluster gas with a standard Beta model. This is highlighted by comparing our central Comptonization results with values calculated from measurements using the BIMA and OVRO interferometers. On average, the SuZIE calculated central Comptonizations are $\sim 60\%$ higher in the cooling flow clusters than the interferometric values, compared to only $\sim 12\%$ higher in the non-cooling flow clusters. We believe this discrepancy to be in large part due to the spatial modelling of the intra-cluster gas. From our cluster sample we construct $y_0$–$T$ and $S$–$T$ scaling relations. The $y_0$–$T$ scaling relation is inconsistent with what we would expect for self-similar clusters;

[1]Department of Physics, 351 LeConte Hall, University of California, Berkeley, CA 94720

[2]Stanford University, 382 Via Pueblo, Varian Building, Stanford, CA 94305

[3]Department of Physics and Astronomy, University of Wales, Cardiff, 5, The Parade, P.O. Box 913, Cardiff, CF24 3YB, Wales, UK

[4]California Institute of Technology, Observational Cosmology, M.S. 59–33, Pasadena, CA 91125

[5]Jet Propulsion Laboratory, 4800 Oak Grove Dr., Pasadena, CA 91109

[6]Infrared Processing and Analysis Center, MS 100-22, California Institute of Technology, Pasadena, CA 91125

[7]Department of Physics, University of California, 1 Shields Avenue, Davis, CA 95616

however this result is questionable because of the large systematic uncertainty in $y_0$. The $S$–$T$ scaling relation has a slope and redshift evolution consistent with what we expect for self-similar clusters with a characteristic density that scales with the mean density of the universe. We rule out zero redshift evolution of the $S$–$T$ relation at $\sim 90\%$ confidence.

*Subject headings:* cosmic microwave background — cosmology:observations — galaxies:clusters:general — large-scale structure of universe

## 1. Introduction

Clusters of galaxies are the largest gravitationally bound objects in the Universe, and formed at relatively early times over a critical redshift range ($0 < z \lesssim 3$) during which the dark energy came to dominate the total energy density of the Universe. A measurement of the evolution of the cluster number density with redshift is sensitive to various cosmological parameters, including $\sigma_8$, $\Omega_M$, $\Omega_\Lambda$, and the dark energy equation of state (Wang & Steinhardt 1998; Holder et al. 2001). A direct measurement of the cluster number density can be made through a survey utilizing the Sunyaev-Zel'dovich (SZ) effect. The SZ effect is particularly well-suited for cluster surveys because an SZ survey will detect every cluster above a mass limit that is independent of redshift (see Carlstrom, Holder, & Reese 2002, for example). Active and planned SZ surveys should result in the discovery of tens of thousands of clusters over the next several years, (see Schulz & White 2003, for a review).

The cosmological constraints from any SZ survey may ultimately be limited by how closely clusters behave as standard candles. Haiman et al. (2001) showed that future SZ surveys are likely to be limited by systematic uncertainties due to the assumption that clusters are virialized objects whose density scales with the mean background density. Observations of relatively nearby clusters ($z \lesssim 0.1$) in X-rays have shown that clusters are at least remarkably regular objects whose observable properties seem to obey well-behaved scaling relations. These scaling relations include the mass-temperature (e.g., Finoguenov et al. 2001), size-temperature (e.g., Mohr et al. 2000), and luminosity-temperature (e.g., Markevitch 1998) scaling relations. Verde et al. (2002) have argued that an integrated SZ flux versus X-ray temperature scaling relation should have an exceptionally small scatter, compared to other cluster scaling relations, and should be especially useful in testing possible deviations from virialization.

Investigations of SZ scaling relations have been limited so far due to a scarcity of measurements. Cooray (1999) and McCarthy et al. (2003) have compiled SZ measurements drawn from the literature and constructed SZ scaling relations; however these studies suffered from several draw-backs. Firstly, both papers drew upon measurements from several different instruments. While no systematic differences across instruments was known of at the time, we believe this paper offers the first evidence that a significant systematic discrepancy does exist. Secondly, both papers concentrated on scaling relations that use the central decrement of the cluster. The calculated central decrement often relies on an assumed spatial distribution of the intra-cluster (IC) gas, whose density is still best constrained by higher resolution X-ray data. The traditional parameterization of the IC gas distribution with the single Beta model (Cavaliere & Fusco-Femiano 1976, 1978) causes a large systematic uncertainty in the central decrement calculated from SZ measurements. In this paper, we address both these issues by constructing scaling relations using SZ measurements from only one instrument, and instead focusing on the integrated SZ flux scaling relation.

In this paper we describe new measurements of the SZ effect towards eight galaxy clusters made with the Sunyaev-Zel'dovich Infrared Experiment (SuZIE). The SuZIE II receiver makes simultaneous measurements of the SZ effect in three frequency bands, centered at 145 GHz, 221 GHz, and 355 GHz, spanning the null of the SZ thermal effect. In combination with previous measurements from the SuZIE instrument, we form a sample of 15 clusters for which we determine the central Comptonization, $y_0$, and integrated SZ flux, $S$. We then use this sample to construct scaling relations between $y_0$ and $S$ and the X-ray temperature and compare these results to theoretical predictions. The layout of this paper is as follows: in §2 and §3 we describe the observations and multi-frequency data analysis. In §4 we describe the analysis to determine the SZ flux. In §5 we compare our SZ measurements to other experiments, particularly from the OVRO and BIMA interferometers. Finally, in §6 we construct SZ scaling relations and compare these measurements with theoretical predictions.

## 2. S-Z Observations

### 2.1. Instrument

We report measurements of the Sunyaev-Zeldovich effect made with the second generation Sunyaev-Zeldovich Infrared Experiment receiver (SuZIE II) at the Caltech Submillimeter Observatory (CSO) located on Mauna Kea. The SuZIE II receiver is a $2 \times 2$ array of three-color photometers that observes the sky simultaneously in three frequency bands. Radiation within each frequency band is detected by a silicon nitride spider-web bolometer cooled to 300 mK (Mauskopf et al. 1997). The bolometer is coupled to the primary mirror by a Winston horn which defines a $\sim 1\farcm5$ FWHM beam on the sky, with each row separated by $\sim 2\farcm3$ and each column by $\sim 5'$ on the sky. The signal from the bolometers in the same row that are sensitive to the same frequency are differenced electronically, equivalent to a square wave chop of $5'$ on the sky. For the new measurements presented in this paper the three frequency bands in each photometer were centered at 145, 221, and 355 GHz with approximately 14%, 11%, and 9% bandwidth respectively. For a more detailed overview of the SuZIE II beam sizes and pass-bands see Benson et al. (2003).

### 2.2. Observations

In addition to the clusters reported in Benson et al. (2003), SuZIE II was used to make observations of an additional eight clusters over the course of four observing runs during December 1998, January 2002, December 2002, and March 2003. These results are summarized in Table 1. We selected bright, known X-ray clusters from the *ROSAT* X-Ray Brightest Abell Clusters (Ebeling et al. 1996a,b) and Brightest Cluster Samples (Ebeling et al. 1998). In particular we selected clusters with published intra-cluster (IC) gas density models and electron temperatures that were previously unobserved with SuZIE, or that had weak peculiar velocity constraints from previous observations. We also observed clusters in directions on the sky largely unobserved by SuZIE in order to have more uniform sky coverage in our search for a local dipole flow (see Benson et al. 2003; Church et al. 2004).

SuZIE II operates in a drift scanning mode, where the telescope is pointed ahead of the source and then parked. The Earth's rotation then causes the source to drift through the array of pixels. Before each scan the dewar is rotated so that the rows of the array lie along lines of constant declination. Each scan lasts two minutes, or $30'$ in right ascension, during which time the telescope maintains a fixed altitude and azimuth. After a scan is complete, the telescope reacquires the source and the scan is then repeated. Keeping the telescope fixed during an observation prevents slow drifts from changes in ground-spillover from contaminating the data. From scan to scan the initial offset of the telescope from the source is alternated between $12'$ and $18'$, allowing a systematic check for an instrumental baseline and a check for any time dependent signals. During the observations presented here, the array was positioned so that one row passed over the center of each cluster, as specified in Table 1.

### 2.3. Calibration

We observe planets for absolute calibration. For the December 1998 and March 2003 observing runs Mars was used as the primary calibrator, for the December 2002 run Uranus was used, and for the January 2002 run Saturn was used.

We observe each primary calibrator at least once a night for absolute calibration of the instrument. We correct for transmission of the atmosphere by measuring the opacity using a 225 GHz tipping tau-meter located at the CSO. During the March 2003 observing run this instrument was not operational: for this run only, we used a scaled 225 GHz optical opacity derived from the 350 $\mu$m tau-meter at the CSO. The opacity at 225 GHz is converted to the opacity in each of our frequency bands by calculating a scaling factor $\alpha_k$ which is measured from sky dips during stable atmospheric conditions. Our responsivity to a celestial source is:

$$R = \frac{I_{\rm plan}\Omega_{\rm plan} \times e^{-\alpha < \tau / \cos\theta_{\rm Cal} >}}{V_{peak}} \left(\frac{\rm Jy}{\rm V}\right) \tag{1}$$

where $\Omega_{\rm plan}$ is the angular size of the planet, and $< \tau / \cos\theta_{\rm Cal} >$ is averaged over the length of the observation, typically less than 20 minutes.

The brightness temperature of Uranus, Saturn, and Mars are all well-studied at millimeter wavelengths. Uranus has been measured at millimeter wavelengths by Griffin & Orton (1993), who model the Uranian temperature spectrum, $T_{\rm Uranus}(\nu)$, with a third order polynomial fit to the logarithm of wavelength. Griffin & Orton report a 6% uncertainty in the brightness of Uranus. Goldin et al. (1997) report RJ temperatures of Saturn in four frequency bands centered between 172 and 675 GHz. From these measurements we fit a second order polynomial in frequency to model $T_{\rm Saturn}(\nu)$. Goldin et al. report a total 5% uncertainty to the brightness of Saturn. We determine the Martian temperature spectrum over our bands from the FLUXES software package developed for the JCMT telescope on Mauna Kea. [1] We fit the temperature spectrum given by FLUXES with a second order polynomial fit to the logarithm of wavelength in order to allow us to interpolate over our frequency range. The reported uncertainty on the Martian brightness temperature is 5%.

Generally it is preferable not to use Saturn as a primary calibrator because of the unknown effect of its ring angle on its millimeter wavelength emission. However, previous SuZIE measurements of Saturn at ring angles between $\pm 9^\circ$ showed a negligible effect on Saturn's millimeter wavelength emission. During the December 2002 run calibration scans were taken of Uranus and Saturn over several nights with Saturn at a ring angle of $\sim -26.6^\circ$. Comparing the scans of the two planets, Saturn was observed to have excess emission by $\sim 72, 43$, and 37% in our 355, 221, and 145 GHz frequency bands. Saturn was not used as a primary calibrator during this run; however due to the lack of any other visible planets, Saturn was the primary calibrator during the January 2002 run when Saturn was at a

[1] http://www.jach.hawaii.edu/JACpublic/JCMT/software/bin/fluxes.pl

ring angle of $\sim -25.8°$. Because the ring angle of Saturn changed by less than a degree between January 2002 and December 2002, we use the cross-calibration of Saturn from Uranus measured in December 2002 to correct the calibration from Saturn for the January 2002 run. For the data presented in this paper, this correction only affects the measurements of MS1054, see Table 1.

Raster scans over Saturn and Mars were used to measure the beam shape during each observing run. In January and December 2002, Saturn was used to measure the beam shape. During these runs Saturn had an angular diameter of $\sim 18.8''$ and $\sim 19.5''$ respectively. In December 1998 and March 2003, Mars was used to measure the beam shape. During these runs Mars had an angular diameter of $\sim 6.0''$ and $\sim 7.2''$, respectively. Compared to our typical beam size of $\sim 90''$, these planets are sufficiently small to be well approximated as point sources.

Including other sources of calibration uncertainty, such as from beam uncertainties and detector non-linearities, we estimate the total calibration uncertainty of SuZIE II in each of its spectral bands to be $\pm 10\%$. For a more thorough overview of the SuZIE II calibration uncertainty see Benson et al. (2003).

## 3. Multi-frequency SuZIE Analysis and Results

Our analysis procedure is described in detail in Benson et al. (2003), but we briefly summarize it in this section. The basic philosophy we use when analyzing SuZIE data is to perform a fit to the data which uses the multi-frequency information to spectrally distinguish between the SZ and atmospheric signal. This procedure has proven invaluable to the analysis of our 355 GHz channel where the atmosphere contributes the largest amount of extra noise.

### 3.1. Defining the Data Set

We will begin by defining some notation to aid in referencing the SuZIE data set. There are two rows of photometers in SuZIE. Each row consists of two photometers separated by $5'$ on the sky, with a photometer consisting of three bolometers each observing at a different frequency. In each row there are six single channel signals, $S$, and three differenced signals, $D$. The difference signals are defined as the difference between the single channel signals of the same frequency band in the same row. We only record three single channel signals from each row, one for each frequency band. We use the subscript $k$ to refer to frequency band, with $k = 1, 2, 3$ referring to the frequency bands of 355, 221, and 145 GHz in the on-source row. We do not include analysis of the data in the off-source row in this paper because it negligibly improves the overall signal to noise. Each two minute scan is broken into forty 3 second bins, with each bin covering a region equal to $0\farcm75 \cos\delta$ on the sky. We will use the subscripts $j$ to refer to scan number, and $i$ to refer to bin number. In this way the difference and single-channel signals at 145 GHz from scan $j$ and bin $i$ in the on-source row are $D_{3ji}$ and $S_{3ji}$.

### 3.2. SZ Model

The spatial model for the expected SZ signal in each scan is calculated from the convolution of the beam map with a model of the opacity of the cluster. A beam map, $V_k(\theta,\phi)$, is measured from raster scans of a planetary calibrator. The optical depth, $\tau$, of each cluster is modelled spatially by a spherically symmetric isothermal $\beta$ model (Cavaliere & Fusco-Femiano 1976, 1978) with

$$\tau(\theta,\phi) = \tau_0 \left(1 + \frac{\theta^2+\phi^2}{\theta_c^2}\right)^{(1-3\beta)/2} \tag{2}$$

where $\theta$ and $\phi$ are angles on the sky and $\beta$ and $\theta_c$ are parameters of the model. Because SuZIE is rotated between scans to match the rotation of the sky, $\theta$ is equivalent to right ascension and $\phi$ to declination. For each cluster the model parameters of the IC gas, $\beta$ and $\theta_c$, are taken from the literature and are listed in Table 2. In this table we also include the clusters previously measured by SuZIE which will be included in our analysis in section 4. We define thermal and kinematic SZ models, $S^{\rm th}(\theta)$ and $S^{\rm kin}(\theta)$, to fit the data with

$$S^{\rm th}(\theta) = T_k m_k(\theta) \tag{3}$$

$$S^{\rm kin}(\theta) = K_k m_k(\theta) \tag{4}$$

where $m_k(\theta)$ is our spatial model, and $T_k$ and $K_k$ are the thermal and kinematic band-averaged spectral factors which are fully specified in Benson et al. (2003). The spatial model, $m_k(\theta)$, is the convolution of the beam-shape, $V_k(\theta',\phi)$, with the cluster optical depth, $\tau(\theta,\phi)$, and has units of steradians. It is calculated at $0'.05 \times cos\delta$ intervals for a given offset, $\theta$, in right ascension from the cluster center. For each cluster the SZ spectral factors, $T_k$ and $K_k$, are calculated assuming the X-ray emission weighted temperature listed in Table 2. With these definitions, $S^{\rm th}(\theta)$ and $S^{\rm kin}(\theta)$ are the thermal and kinematic SZ signal we expect to see in frequency band $k$ in a scan across a cluster of unity central Comptonization, $y_0$, with a radial component to the peculiar velocity, $v_p$, of $1\,{\rm km\,s^{-1}}$. The calculated SZ model is then combined into $0'.75 \times \cos\delta$ bins to match the binned SuZIE II data, so that we define $S^{\rm th}_{ki}$ as the thermal SZ model in channel $k$ for the right ascension offset $\theta$ of bin number $i$.

### 3.3. Atmospheric Noise Templates

There are two sources of residual atmospheric noise in our difference channels. First there is a residual common signal to each beam due to the finite common-mode rejection ratio (CMRR) of the electronic differencing, and second there is a residual differential atmospheric signal introduced because the two differenced beams pass through slightly different columns of atmosphere. We model the residual common atmospheric signal, $C_{kji}$, in each frequency band by the corresponding single channel signal, $S_{kji}$. We model the residual differential atmospheric signal, $A_{ji}$, in each row by forming a linear combination of the differential channels that contains no residual SZ signal. We define $A_{ji} \equiv \alpha D_{1ji} + \gamma D_{2ji} + D_{3ji}$, with the coefficients $\alpha$ and $\gamma$ chosen to minimize the residual thermal and kinematic SZ flux in $A_{ji}$. In Benson et al. (2003) the exact method to calculate $\alpha$ and $\gamma$ is explained in detail. We list the values of $\alpha$ and $\gamma$ for each cluster in Table 3. The values of $\alpha$ and $\gamma$ are similar between clusters, but vary somewhat due to differences in their intra-cluster gas model and electron temperature.

### 3.4. Fitting for the Cluster Center

The location of the cluster in the scan is another free parameter for which we can fit. Before fitting for the cluster location we perform an initial "cleaning" of each scan of each frequency channel by removing the best-fit slope, constant offset, and a signal proportional to the common and differential atmospheric signal. The individual scans from each frequency channel are then co-added, weighted by the root-mean squared of the residual of the scan. The "cleaned" co-added scan from the on-source row at $\nu \sim 145\,\mathrm{GHz}$ ($k = 3$) is then fitted with a model that includes a slope, an offset, and the SZ model, where the cluster location and the central Comptonization are allowed to vary. The best-fit cluster location, quantified as a right ascension offset, $\mathrm{RA}_{\mathrm{offset}}$, from the pointing center, is then used to fix the cluster location for the rest of our analysis. The values of $\mathrm{RA}_{\mathrm{offset}}$ for each cluster are listed in Table 4. The nominal pointing center of each cluster is defined from its respective X-ray centroid.

It is noted that from SuZIE data alone we can only constrain the cluster's location in right ascension. The combined pointing uncertainty from the CSO and the X-ray data is $\sim 20''$ and, in general, is expected to have minimal effect on our results due to the relatively large size, $\sim 90''$, of SuZIE's beams. In fact in Benson et al. (2003) it was shown that a 20" pointing offset corresponded to only a $\sim$4% overestimate of the central Comptonization, generally a negligible correction compared to the statistical uncertainties in our measurements. For a more detailed discussion of the pointing uncertainty and its effect on our results see Benson et al. (2003).

The clusters observed in March 2003 all lie within 30" of the nominal pointing center, however both clusters observed during December 2002, A520 and A2390, are significantly off center. The measured right ascension offset for A520 was $103^{+51}_{-53}$" and for A2390 was $-60^{+28}_{-29}$". Because the offsets have a different sign it is unlikely there was a systematic offset in our pointing consistent across the sky. In previous results, no pointing error of this magnitude had been observed, of the eight cluster observations reported in Benson et al. (2003) all lie within 30" of their nominal pointing centers. We now discuss the apparent discrepancy of the cluster location of A520 and A2390 individually.

In Table 5 we give the location of A520 from two different X-ray measurements and from our SuZIE observation. The X-ray measurements are described in Ebeling et al. (1998) and Allen (2000), with the respective locations calculated from the X-ray centroid. No uncertainties were given for either X-ray measurement, however the typical pointing uncertainty of ROSAT is $\sim 10''$ while the spatial resolution of the PSPC is $\sim 30''$ and the HRI is $\sim 2''$. The pointing center for the SuZIE observation of A520 was defined as the X-ray centroid of the PSPC. It can be seen in Table 5 that the X-ray centroid from the HRI is more consistent with the location measured by SuZIE than the PSPC observation which had defined our pointing center. In addition, an observation of A520 by the OVRO interferometer measured a cluster location consistent with the location measured by SuZIE (Reese 2003). This could suggest that the X-ray and SZ centroid may not be equivalent for this cluster. For these reasons, we believe the pointing offset observed by the SuZIE observation of A520 is a real effect and consistent with the true SZ center.

In Table 5 we give the location of A2390 based on two different X-ray measurements and two different SuZIE observations. The X-ray references for A2390 are the same as for A520, and determine the cluster location from the position of the X-ray centroid. The X-ray centroid measured from the PSPC and from the HRI agree very well. Because the HRI has a much finer spatial resolution than the PSPC, see the preceding paragraph, we will only consider the more certain HRI coordinates. The SuZIE observation from November 2000 measured a best-fit location nearly coincident with the HRI X-ray centroid, while the SuZIE observation from December 2002 measured a best-fit location $\sim$ 60" west. The 68% confidence intervals do not overlap between the measurements, however they are only separated by $\sim$ 9". Because we had not previously observed any pointing offset and A2390 had been successfully observed with SuZIE before in November 2000, we analyze the A2390 measurements from December 2002 assuming zero offset from the nominal pointing center. This adjustment changes the calculated central Comptonization of A2390 by only $\sim$3% when considering the combined results of the November 2000 and December 2002 observing runs which is calculated in section 3.5.

### 3.5. Individual Scan Fits for the Central Comptonization

To determine our best-fit results and formal confidence intervals for the central Comptonization of each cluster, we have adopted the approach of fitting all three frequency channels on a scan-by-scan basis. From the raw binned calibrated data, $D_{kji}$, we expect our signal to consist of a DC offset, a slope, a signal proportional to our model of the residual common and differential atmospheric signals, and a thermal and kinematic SZ model, with a central Comptonization and peculiar velocity fixed between frequency bands. The residual signal, $R_{kji}$, after removal of these signals is then

$$R_{kji} = D_{kji} - a_{kj} - ib_{kj} - (e_{kj} \times C_{kji}) - (f_{kj} \times A_{ji}) - y_{0j} T_k m_k(\theta_i - \mathrm{RA}_{\mathrm{offset}}) - (y_0 v_p)_j K_k m_k(\theta_i - \mathrm{RA}_{\mathrm{offset}}) \tag{5}$$

where $a_{kj}$ are the offset terms, $b_{kj}$ are the slope terms, and $e_{kj}$ ($f_{kj}$) are the coefficients that are proportional to the common-mode (differential-mode) atmospheric signal in frequency channels $k = 1, 2, 3$. The SZ-model parameters $y_{0j}$ and $(y_0 v_p)_j$ are proportional to the magnitude of the thermal and kinematic components in each frequency channel. The best-fit model of scan $j$ is then determined by minimizing the $\chi^2$ as defined in Benson et al. (2003). The uncertainty of the fit parameters are determined using the standard definition from a general linear least-squares fit (see Press et al. 1992, for example).

From the individual scan fits we construct a 2 by 2 symmetric covariance matrix, $\Sigma$, from each scan's fit for central comptonization and peculiar velocity, see Benson et al. (2003) for our exact definition of $\Sigma$. Having calculated the covariance matrix, we perform a maximum likelihood analysis for the model parameters $y_0$ and $v_p$ with our likelihood function defined as

$$L(v_p, y_0) = \frac{1}{(2\pi)|\mathbf{\Sigma}|^{1/2}} \exp\Big[ -\frac{1}{2} \begin{pmatrix} <y_0> - y_0 \\ <y_0 v_p> - y_0 \times v_p \end{pmatrix}^T \mathbf{\Sigma}^{-1} \begin{pmatrix} <y_0> - y_0 \\ <y_0 v_p> - y_0 \times v_p \end{pmatrix} \Big] \tag{6}$$

where $< y_0 >$ and $< y_0 v_p >$ are weighted averages of the individual scan fits for the thermal and kinematic SZ components, and are defined as

$$< y_0 > = \frac{\sum_j^{N_s} y_{0j}/\sigma_{yj}^2}{\sum_j^{N_s} 1/\sigma_{yj}^2} \tag{7}$$

$$< y_0 v_p > = \frac{\sum_j^{N_s} (y_0 v_p)_j/\sigma_{(y_0 v_p)j}^2}{\sum_j^{N_s} 1/\sigma_{(y v_p)j}^2} \tag{8}$$

We calculate our formal confidence intervals for $y_0$ by marginalizing $L(v_p, y_0)$ over the peculiar velocity. See Table 4 for the $y_0$ results for each new cluster presented in this paper. The constraints on each cluster's peculiar velocity will be the subject of a future paper. In Table 6 we give a summary of the $y_0$ results calculated from a marginalization of $L(v_p, y_0)$ for all the clusters which have multi-frequency information from SuZIE.

Of the new measurements presented in this paper, only A2390 had been observed previously by SuZIE. It is worthwhile to compare the December 2002 results to the previous observation from November 2000 for a systematic check of any time-dependent or observing-dependent errors. In Figure 1 we plot the 2-d likelihoods from both observing runs, and their product. It is evident that the overall constraints from the November 2000 data are much weaker. Due to the low sensitivity of this data, there is a very weak constraint on the peculiar velocity and a large degeneracy towards an increasing peculiar velocity and a decreasing Comptonization. The 68% confidence regions do overlap between the two data sets, and we consider them in good agreement. The combined likelihood for A2390 is the product of the likelihoods from the November 2000 and December 2002 observing runs, $L(v_p, y_0) = L(v_p, y_0)_{\rm Nov00} \times L(v_p, y_0)_{\rm Dec02}$. For A2390, the value of $y_0$ given in Table 6 is calculated from marginalizing the combined likelihood function over peculiar velocity.

### 3.6. Spectral Plots for Each Cluster

In order to visualize the SZ spectrum measured by SuZIE we calculate intensities from the co-additions of the differenced data in each frequency band. It should be noted, that the calculated intensities and respective uncertainties given in this section should not be used on their own due to the correlated noise between frequency bands introduced by our atmospheric subtraction method. However, the best-fit intensities are an accurate measurement of the correct intensity at each frequency, and are meant to visually verify that we do measure an SZ-like spectrum.

We begin with our cleaned data set, $Y_{kji}$, defined as

$$Y_{kji} = D_{kji} - a_{kj} - ib_{kj} - (e_{kj} \times C_{kji}) - (f_{kj} \times A_{ji}) \tag{9}$$

with the best-fit parameters for $a_{kj}$, $b_{kj}$, $e_{kj}$, and $f_{kj}$ determined from equation (5). This cleaned data set can now be co-added using the RMS of $R_{kji}$, from equation 5, as a weight, such that:

$$Y_{ki} = \frac{\sum_{j=1}^{N_s} Y_{kji}/\mathrm{RMS}_{kj}^2}{\sum_{j=1}^{N_s} 1/\mathrm{RMS}_{kj}^2} \tag{10}$$

with $\mathrm{RMS}_{kj}^2 \equiv \sum_i^{N_b}(R_{kji})^2/(N_b - 1)$. The RMS of $R_{kji}$ is not biased by any contribution from the SZ source. The uncertainty of each co-added bin, $\sigma_{ki}$, is determined from the dispersion about the mean value, $Y_{ki}$, weighted by $\mathrm{RMS}^2_{kj}$,

$$\sigma_{ki} = \sqrt{\frac{\sum_{j=1}^{N_s} (Y_{ki} - Y_{kji})^2/\mathrm{RMS}^2_{kj}}{(N_s - 1)\sum_{j=1}^{N_s} 1/\mathrm{RMS}^2_{kj}}} \tag{11}$$

The best-fit central intensity, $I_k$, for each frequency band is then found by minimizing the $\chi^2_k$ of the fit to the co-added data, where $\chi^2_k$ is defined as follows:

$$\chi^2_k = \sum_{i=1}^{N_b} \frac{[Y_{ki} - I_k \times m_k(\theta_i - \mathrm{RA}_{\mathrm{offset}})]^2}{\sigma^2_{ki}} \tag{12}$$

We calculate the confidence intervals for $I_k$ under the assumption of Gaussian errors on $Y_{ki}$ where our likelihood function is related to the $\chi^2$ via $L(I_k) \propto \exp(-\chi^2_k/2)$.

Figure 2 plots the best-fit SZ spectrum with the measured intensities overlaid for the entire sample of 11 clusters detected in multiple frequency bands by SuZIE II. This plot includes cluster spectra given in Benson et al. (2003), along with the new results from clusters observed in the December 2002 and March 2003 observing runs. For clusters detected in multiple observing runs, such as for MS0451 and A2390, the intensity points are calculated by multiplying the likelihoods in intensity space, $L(I_k)$, from each observing run for each respective frequency band.

## 4. 145 GHz SuZIE Analysis and Results

Ultimately we wish to compare our results for the central Comptonization to independent single frequency SZ measurements, which by themselves cannot constrain the peculiar velocity. In principle, our multi-frequency results should be an appropriate comparison because they take full account of the shape of the SZ spectrum and should therefore accurately measure Comptonization. However, there are some advantages in considering the 145 GHz data on its own. The 145 GHz channel is the most sensitive of the frequency channels to the SZ thermal effect. Including the higher frequency channels allows one to constrain the peculiar velocity as well as the central Comptonization. However, due to the lower sensitivity of the higher frequency channels and the addition of the peculiar velocity as a free paramater, the overall constraints on the calculated central Comptonization actually decreases with the addition of the higher frequency channels. In addition, the higher frequency channels suffer more confusion from sub-millimeter point sources. We showed in Benson et al. (2003) that typical sub-millimeter point sources in our cluster fields have a tendency to bias our peculiar velocity results towards negative values by a factor of several hundred kilometers per second and our central Comptonization results higher by several times $10^{-4}$. This effect can be minimized by only analyzing the 145 GHz data because sub-millimeter point sources have spectral energy densities which decrease with frequency. For these reasons, it is useful to analyze the cleaned co-added 145 GHz data alone, which will be the subject of this section. For this analysis we include previous SuZIE measurements given in Holzapfel et al. (1997b) and Benson et al. (2003) as well as the measurements given in this paper.

### 4.1. Fitting for a Central Comptonization

We calculate a central Comptonization from the co-added 145 GHz data using a method similar to the one used to calculate the intensity points in section 3.6 except here we are solving for a central Comptonization instead. For our data, we use the co-added scan from the on-source row at 145 GHz, $Y_{3i}$, which was defined in equation 10. From $Y_{3i}$ we subtract a SZ model which includes a peculiar velocity, $v_p$, and a central Comptonization, $y_0$, to calculate a $\chi^2$ which we define as

$$\chi^2(v_p, y_0) = \sum_{i=1}^{N_b} \frac{\left[Y_{3i} - y_0 m_3(\theta_i - \mathrm{RA}_{\mathrm{offset}})(T_3 + v_p K_3)\right]^2}{\sigma_{3i}^2} \tag{13}$$

where $T_3$, $K_3$, and $m_3(\theta)$ are defined in section 3.2. Under the assumption of Gaussian errors on $Y_{3i}$, this $\chi^2$ is related to the likelihood via $L(v_p, y_0) \propto \exp(-\chi^2(v_p, y_0)/2)$. In this work we are interested only in the central Comptonization, and so marginalize over the peculiar velocity. We assume a Gaussian prior on $v_p$ whose likelihood we take to be $\propto \exp(-v_p^2/2\sigma_v^2)$. For these measurements we assume a most-likely peculiar velocity of $v_p = 0$ km s$^{-1}$ and a Gaussian width $\sigma_v = 500$ km s$^{-1}$. Because the clusters peculiar velocities are expected to be randomly distributed around $v_p = 0$ km s$^{-1}$, this assumption should not bias these results. We marginalize over peculiar velocity such that our formal probability distribution for the central Comptonization, $P(y_0)$, is defined as

$$P(y_0) = \frac{1}{\sqrt{2\pi\sigma_v^2}} \int L(v_p, y_0) \exp\left(\frac{-v_p^2}{2\sigma_v^2}\right) dv_p \tag{14}$$

From $P(y_0)$ we calculate our best-fit central Comptonization and associated 68% confidence region for the 15 clusters presented in this paper, Benson et al. (2003), and Holzapfel et al. (1997b). For a summary of these results see Table 7.

With currently favored cosmological models it is expected that the peculiar velocities of clusters be less than 1000 km s$^{-1}$ (Gramann et al. 1995; Sheth & Diaferio 2001; Suhhonenko & Gramann 2003). However recent observations show evidence for internal flows as large as $4000\,\mathrm{km\,s^{-1}}$ (Dupke & Bregman 2002; Markevitch et al. 2003). Therefore it is expected that the $\sigma_v = 500\,\mathrm{km\,s^{-1}}$ prior is a reasonable estimate of the true width, however larger velocities have not been observationally ruled out. Because the multi-frequency results from SuZIE constrain the peculiar velocity through the measurement of the SZ spectrum, we will consider a broader range of priors on the peculiar velocity when we re-analyze these results in section 5.2. There we will show that broadening this prior to include larger peculiar velocities with greater probability does not greatly affect the results. However for the 145 GHz data analysis we only consider the case where $\sigma_v = 500\,\mathrm{km\,s^{-1}}$.

If we compare the central Comptonizations calculated from the 145 GHz data, given in Table 7, to those calculated from the multi-frequency data, given in Table 6, it is clear that the 145 GHz results give better constraints for the central Comptonization. While it may seem counterintuitive that the exclusion of two frequency channels actually increases the constraints on the central Comptonization, this gain occurs because of the way we handle the cluster peculiar velocity in both calculations. For the 145 GHz analysis we placed a Gaussian prior of width 500 km $\mathrm{s^{-1}}$ on the peculiar velocity. However, for the multi-frequency analysis in section 3.5, we placed no prior on the peculiar velocity, adding a degree of freedom to the analysis. In fact, the multi-frequency constraints on peculiar velocity are $\sim 1000 - 2000$ km $\mathrm{s^{-1}}$ (Benson et al. 2003; Church et al. 2004), which is less constraining than the prior we used in the 145 GHz analysis. Because the higher frequency channels are also less sensitive to the SZ thermal effect than the 145 GHz channel, the overall effect is that the 145 GHz results more tightly constrain the central Comptonization than the multi-frequency results.

It should be noted that for the clusters from Holzapfel et al. (1997b), A1689 and A2163, the IC gas model used by Holzapfel et al. (1997b) differed from those used in Reese et al. (2002). In Table 8 we give a summary of the beta models and electron temperatures used in both references. We also give the calculated central Comptonization derived from the SuZIE measurements using the two sets of IC gas models. For the case of A1689 the difference in beta model parameters was significant. This is not surprising considering the gas model used by Holzapfel et al. (1997b) for A1689 was calculated from an unpublished analysis of a PSPC observation, while the model used by Reese et al. (2002) was calculated from a more recent HRI observation. For the A1689 SuZIE results, the model assumed significantly changes the calculated central Comptonization, by $\sim 40\%$. This difference is largely because A1689 is unresolved by SuZIE, and therefore the central Comptonization calculated depends entirely on the assumed IC gas model. To maintain consistency with Reese et al. (2002), the central Comptonizations of A1689 and A2163 given in Table 7 assume the IC gas model parameters used in Reese et al. (2002). Because all of the clusters observed by SuZIE are unresolved the calculated central Comptonization depends sensitively on the assumed IC gas model, this uncertainty will be discussed further in section **??**.

### 4.2. Fitting for the Integrated SZ Flux

In the last section, it was shown that the inferred central Comptonization for A1689 changes significantly depending on the IC gas model assumed. It would be preferable to express our SZ measurements in a way that depends less sensitively on the assumed IC gas model. An alternative observable is the SZ flux integrated over some well-defined area on the sky. In the literature, this area is usually defined by the radius at which the mean over-density of the cluster is equal to some factor, $\Delta$, times the critical density of the universe at that redshift, $\rho_{\rm clust}(r_\Delta) = \rho_{\rm crit}(r_\Delta)\Delta$. For X-ray measurements the value of $\Delta$ is usually chosen in a range between 500 and 2500 because the intra-cluster gas is expected to be virialized within this range of radii (Evrard et al. 1996). In this paper we adopt $\Delta = 2500$ with the $r_{2500}$ calculated for each cluster given in Table 9. For this choice of $\Delta$, $r_{2500}$ is less than the SuZIE 5' difference chop, assuming a standard $\Lambda$CDM cosmology, for each cluster. In this section we will detail our calculation of the integrated SZ flux within $r_{2500}$, $S(r_{2500})$.

The total mass of a cluster whose gas distribution is described by an isothermal $\beta$ model can be calculated, under the assumption of hydrostatic equilibrium and spherical symmetry, such that the total mass within a radius, $r$, is

$$M_{\rm clust}(r) = \frac{3kT_e\beta}{G\mu m_p}\frac{r^3}{r_c^2 + r^2} \tag{15}$$

where $T_e$ is the cluster's electron temperature, $\mu m_p$ is the mean molecular weight of the gas where we assume $\mu = 0.6$, with $\beta$ and $r_c$ corresponding to the $\beta$ model parameters for the cluster. The cluster mass can be related to the critical density of the universe, $\rho_{\rm crit}$, by

$$M_{\rm clust}(r_\Delta) = \rho_{\rm crit}(z)\frac{4\pi r_\Delta^3}{3}\Delta \tag{16}$$

where $\rho_{\rm crit}(z) = 3H(z)^2/(8\pi G)$, $H(z)$ is the Hubble constant at a redshift $z$, $G$ is the Gravitational constant, $r_\Delta$ is some radius of the cluster, and $\Delta$ is the constant which makes this expression true. For reasons given at the beginning of this section we adopt $\Delta = 2500$. Equation 16 can be re-arranged to solve for $r_{2500}$ with

$$r_{2500} = \left[\frac{6}{2500}\frac{kT_e\beta}{\mu m_p}\frac{c^2}{H_0^2 E(z)^2} - r_c^2\right]^{1/2} \tag{17}$$

where the variables are previously defined and where we have replaced $H(z)^2 = E(z)^2 H_0^2$ with $E(z)^2 \equiv \Omega_M(1+z)^3 + (1 - \Omega_M - \Omega_\Lambda)(1+z)^2 + \Omega_\Lambda$. We can then define the integrated flux as

$$S(r_{2500}) = y_0 T_k \int_0^{r_{2500}/d_A} 2\pi\theta \left(1 + \frac{\theta^2}{\theta_c^2}\right)^{(1-3\beta)/2} d\theta \tag{18}$$

where $y_0$ is the central Comptonization, $T_k$ is the thermal SZ band-averaged spectral factor used in equation 5 and fully specified in Benson et al. (2003), $\theta_c$ and $\beta$ are the IC gas model parameters, and $d_A$ is the angular diameter distance to the cluster. We note that $T_k$ depends on the cluster electron temperature due to relativistic corrections to the SZ spectrum. For the current SuZIE II 145 GHz (k=3) bandpass $T_3 = A \times 2(kT_{\rm CMB})^3/(hc)^2$ where $A = -3.93$ in the non-relativistic limit and varies between $-3.6$ and $-3.8$ over our typical range of electron temperatures.

We assume the following in our calculation of $S(r_{2500})$ from equation 18. For all the clusters in our sample, we have assumed the 145 GHz (k=3) band for the current SuZIE instrument, and we use the central Comptonization results which were calculated in section 4.1, whose values are given in Table 7. For all clusters we assume the IC gas model parameters given in Table 2. More precisely, for the non-cooling flow clusters we use the X-ray emission weighted temperatures, and for the cooling flow clusters we use the X-ray temperatures which account for the presence of the cooling flows. It is well-known from X-ray measurements, that cooling flows bias X-ray measured temperatures low compared to the virial temperature of the IC gas (see Allen & Fabian 1998, for example). The central Comptonization results given in section 4.1 assume the standard X-ray emission weighted temperature, even for the cooling flow clusters, however we will show in section 4.4 that this correction is negligible compared to the statistical uncertainty in our results. Making the above assumptions we calculate $S(r_{2500})$ for each cluster, these results are given in Table 9.

The error bars for $S(r_{2500})$ given in Table 9 are calculated from the statistical uncertainty in $y_0$ and $T_e$ added in quadrature according to equation 18. In general, the statistical uncertainty in $y_0$ dominates the total uncertainty in $S(r_{2500})$. For example, in the case of RXJ1347, the overall uncertainty in $S(r_{2500})$ is $\sim$ 35mJy with the temperature uncertainty contributing an uncertainty of $\sim$ 8mJy in $S(r_{2500})$, which when added in quadrature is negligible. However, several clusters have significantly less constrained electron temperatures, particularly those clusters with cooling flow corrected temperatures based on ASCA data, for which the temperature uncertainty is a significant contribution to the overall uncertainty in $S(r_{2500})$.

### 4.3. Systematic Effects from an Uncertain Beta Model

In order to examine the effect of an uncertain Beta model on our 145 GHz results, we have calculated the central Comptonization, and the integrated SZ flux out to $r_{2500}$ for a range of Beta models for two of our clusters, A1689 and A1835. We have chosen these clusters because they are cooling flow clusters, whose X-ray emission, in general, is not as well characterized by a spherical isothermal Beta model. In addition, both clusters have at least two published Beta gas models derived from different X-ray instruments sensitive to different spatial scales. One of the systematic effects that we are primarily concerned about in using X-ray models to fit SZ observations is that the X-ray Beta models might over-fit to the cooling core for cooling flow clusters. This is a result of X-ray observations being more sensitive to over-densities in the core of a cluster than SZ observations, because $L_X \propto n_e^2$ while $I_{SZ} \propto n_e$. By choosing models derived from X-ray data which either do not resolve the cooling core, or exclude it entirely in the spatial fit, we can get some idea of the range of derivable Beta models from X-ray data for both clusters.

Figure 3 shows the calculated central Comptonization, $y_0$, and integrated SZ flux, $S(r_{2500})$, for A1835, assuming a suitable range of Beta models. In the figure the asterisk denotes the Beta model given in Reese et al. (2002), derived from ROSAT-HRI data, and the plus sign denotes the Beta model given in Majerowicz et al. (2002), which was derived from observations with XMM and excluded the central region of the cluster out to a radius of 42 arcsec. The choice of Beta model causes nearly a factor of 2 difference in the calculated central Comptonization between the two IC gas models. However, $S(r_{2500})$ varies by $\lesssim 3\%$ between the same models, with the line which connects the two models nearly lying along a line of constant integrated flux.

Figure 4 shows the calculated central Comptonization, $y_0$, and integrated SZ flux, $S(r_{2500})$, for A1689, assuming a suitable range of Beta models. In the figure the asterisk denotes the Beta model given in Reese et al. (2002), derived from ROSAT-HRI data, and the plus sign denotes the Beta model given in Holzapfel et al. (1997b), derived from ROSAT-PSPC data. Again, which IC gas model is assumed significantly changes the calculated central Comptonization, by $\sim 40\%$, however between the two models $S(r_{2500})$ varies by $\lesssim 2\%$.

As we have seen, for both A1835 and A1689 the calculated central Comptonization is much more sensitive to the assumed Beta model than is the integrated SZ flux. The physical reason why this is true is because both clusters are unresolved by SuZIE and therefore the calculated central Comptonization depends entirely on the assumed IC gas model. Conversely, $S(r_{2500})$ is less sensitive to the assumed IC gas model because $r_{2500}$ is well-matched to the SuZIE beam-size, with $r_{2500}$ within a factor of $\sim 2$ of the SuZIE beam-size for all our clusters. For our two example clusters, A1835 and A1689, $S(r_{2500})$ varies by $\lesssim 3\%$ even when significantly different Beta models derived from X-ray measurements with different spatial resolutions are used. The results for A1835 and A1689 imply that even if the X-ray IC gas model over-fits to the cooling core, this does not have a significant systematic effect on the value of $S(r_{2500})$ derived from the SuZIE measurements. We therefore conclude that the choice of Beta model adds a negligible uncertainty to $S(r_{2500})$ when compared to the statistical uncertainty of our data.

We should note that extending our integrated flux calculations to larger radii potentially increases the systematic error in the integrated SZ flux result. For the two clusters above, A1835 and A1689, increasing the integrating radius to $r_{500}$ also increases the difference between $S(r_{500})$ derived from their two respective published IC gas models. For A1835 and A1689 the magnitude of $S(r_{500})$ decreases by $\sim$ 6% and $\sim$ 16%, respectively, when using the broader core radius Beta model, relative to the narrower core radius model, for each cluster. This difference is not surprising considering $r_{2500}$ is already greater than the SuZIE beam-size for most of our clusters, see Table 9, with $r_{500}$ generally a factor of $\sim$2 larger than $r_{2500}$ for a typical cluster. Regardless, there seems to be a systematic trend towards over-estimating the integrated SZ decrement out to $r_{500}$ by $\sim$ 5-20% when using the narrower core radius models for cooling flow clusters. This level of uncertainty is approximately equal to the statistical uncertainty of our measurements, and should be considered when extrapolating our integrated SZ flux measurements to larger cluster radii.

### 4.4. Systematic Effects from an Uncertain Electron Temperature

To examine the effect of an uncertain electron temperature on the SuZIE results we consider two different possibilities. First, we consider a model with a non-isothermal temperature structure implied from XMM measurements for one of our cooling flow clusters, A1835. Secondly, we consider the effect of a significant systematic bias in the assumed isothermal electron temperature.

#### *4.4.1. Non-Isothermal Temperature Structure*

A previous SuZIE paper by Holzapfel et al. (1997a) used a more complicated cluster thermal structure, suggested from ASCA observations, to analyze their 145 GHz results and found that the value of the central Comptonization was relatively insensitive to the details of the thermal structure. With the current generation of X-ray telescopes, XMM and Chandra, there exists a greater capability to resolve cluster temperature structure. Of the clusters in our sample, A1835 has several published X-ray results from XMM and Chandra (Peterson et al. 2001; Majerowicz et al. 2002, for example). In particular Majerowicz et al. (2002) used XMM observations to measure a radial temperature profile in 6 annuli out to a radius of 6', or $\sim 3r_{2500}$. Using a more realistic temperature profile for one of our cooling flow clusters is of particular interest because of the well-known drop in temperature in the central core of the cooling flow. To this end, we have adopted the radial temperature profile given in Majerowicz et al. (2002) and re-analyzed our results for A1835 to study the effect of a non-isothermal temperature structure.

In Table 10 we give the temperature profile of A1835 given in Majerowicz et al. (2002). The XMM observations did not have sufficient sensitivity beyond a radius of 6' to significantly measure the cluster temperature. Little is known about the temperature structure in the outer most regions of clusters, although it is expected the temperature will decrease at some radius. We will assume beyond 6' the cluster is isothermal with a temperature of 7.6 keV, which is the mean temperature outside the cooling flow calculated by Majerowicz et al. (2002). While this is a fairly arbitrary assumption, we will later show that the assumed value only weakly affects our results.

In Table 11 we give the calculated central Comptonization and the integrated SZ flux assuming the above temperature profile and the Beta model parameters given in Table 2. We give results for both the multi-frequency analysis and the 145 GHz analysis, which were described in sections 3.5 and 4.1 respectively. For comparison, we list the results from sections 3.5 and 4.1 which assumed an isothermal intra-cluster gas with $kT_e = 8.2$ keV. For both analysis methods the calculated central Comptonization and integrated SZ flux change negligibly between the above two temperature models compared to the statistical uncertainty of our measurements. This suggests that our results are largely insensitive to the detailed thermal structure of the gas, and are particularly insensitive to the cool core in cooling flow clusters. To examine the effect of the unknown temperature in the outer region of the cluster, in Table 11 we also give our results using the XMM thermal model but instead assuming a temperature of 4.11 keV beyond a radius of 6 '. Comparing the results assuming this model with those which assumed an isothermal 8.2 keV gas, the results again change negligibly compared to the statistical uncertainty of our measurements. In addition, the results of the two XMM models in Table 11 are nearly identical. Considering we changed the temperature of the outer region by nearly a factor of two, this suggests that whatever reasonable temperature we might assume for the outer region would not have a significant effect on our results. Therefore we conclude that the thermal structure of the intra-cluster gas adds a negligible uncertainty to our results.

#### *4.4.2. Systematic Bias in the Assumed Isothermal Temperature*

We now consider the case of a significant systematic bias in the assumed isothermal electron temperature greater than the quoted statistical uncertainty. To some degree a systematic bias in the electron temperature is expected due to any difference between the X-ray derived temperature and the mass weighted temperature, which is relevant for SZ observations. Simulations by Mathiesen & Evrard (2001) predict that temperatures derived from spectral fits to X-ray data are $\sim$ 1-3keV less than the mass weighted temperature, with the systematic offset proportional to the temperature of the cluster. Here we discuss the effect of a systematic bias in the temperature on the calculated central Comptonization and the integrated SZ flux.

We can again consider the case of A1835, one of our more significant detections, to examine the effect of a systematic temperature uncertainty on the central Comptonization. Mathiesen & Evrard (2001) suggests that in the most extreme cases the mass weighted temperature is $\sim$40% higher than the X-ray spectral temperature. For A1835 a 40% offset in temperature corresponds to a temperature of $\sim$11.5 keV. In Table 11 we give our results for A1835 using both the multi-frequency analysis and the 145 GHz analysis, which were described in sections 3.5 and 4.1 respectively, assuming an isothermal temperature of 11.5 keV. Both the multi-frequency and 145 GHz results do not change significantly compared to the results which assumed an isothermal temperature of 8.2 keV. In Table 11 we also give the results for A1835 assuming an isothermal temperature of 4.11 keV, the temperature Majerowicz et al. (2002) measured for the cluster core. While X-ray observations strongly suggest that most of the cluster gas is well above this temperature, our results do not significantly change even with this most pessimistic assumption for the temperature. Overall, in Table 11 our results change remarkably insignificantly over a relatively extreme range of temperatures. This insensitivity is because the calculated central Comptonization depends on the temperature through relativistic corrections to the SZ spectrum, which are still relatively small at 145 GHz for a reasonable range of temperatures. We conclude that any uncertainty in the electron temperature causes a negligible contribution to the uncertainty of our results for all the clusters in our sample.

We should note that if we had allowed $r_{2500}$ to vary with the temperature according to equation 17, the results in Table 11 for the integrated flux, $S(r_{2500})$, would have changed significantly. Our definition of the integration cut-off radius, $r_{2500}$, goes approximately like $T_e^{1/2}$, which in turn causes a dependence of the integrated SZ flux, $S(r_{2500})$, on temperature through the integral in equation 18. Therefore a systematic bias in the definition of the X-ray temperature across all our clusters would tend to affect our integrated SZ flux results somewhat proportionally. While this would have the potential to bias our scaling relation calculations later in section 6, it would not necessarily be evident in our relations through excess scatter. Regardless, for comparison purposes it is useful to use the same definition of $r_{2500}$ calculated from the X-ray temperature which is used to calculate the analogous X-ray scaling relations. For this reason we do not consider the effect of a systematic uncertainty in the electron temperature on $S(r_{2500})$ through the definition of $r_{2500}$, except to note that a systematic bias could exist in the X-ray determined electron temperatures, and generally should be considered when interpreting our results.

## 5. Comparison of SZ Measurements with Previous Results

In total the SuZIE observing program has detected the SZ spectrum of 13 clusters of galaxies and detected an SZ decrement in 15 clusters of galaxies, see Holzapfel et al. (1997b); Benson et al. (2003), and this paper. An important systematic check is to compare our results to SZ measurements using other instruments. The most comprehensive set of SZ measurements published are those by Reese et al. (2002) using the Berkeley-Illinois-Maryland Association (BIMA) and Owens-Valley Radio Observatory (OVRO) millimeter wavelength interferometers. A total of 10 clusters overlap between the SuZIE cluster sample and the set published in Reese et al. (2002). In this section we derive a central Comptonization for each of the 10 overlapping clusters published in Reese et al. (2002) and compare these values for the calculated central Comptonizations from SuZIE. To simplify the comparison of these clusters we have used the same IC gas model as Reese et al. (2002) to analyze our measurements.

### 5.1. BIMA and OVRO

The BIMA and OVRO arrays are millimeter wavelength interferometers, which have been outfitted with centimeter wavelength receivers to observe the SZ effect. The receivers use High Electron Mobility Transistor (HEMT) amplifiers which are used to observe the SZ effect in a band between 28-30 GHz. At this observing frequency the primary beams for each interferometer are nearly Gaussian with a FWHM of 6.6' for BIMA and 4.2' for OVRO. The angular resolution varies depending on the configuration of the dishes during each particular observation, but is typically $\sim 95 \times 95$ arcsec for BIMA and $\sim 50 \times 50$ arcsec for OVRO. For an overview of the interferometers and the SZ observations using them see Reese et al. (2002).

#### *5.1.1. Fitting a Central Comptonization to the BIMA and OVRO Data*

The BIMA and OVRO interferometers observe the SZ effect in a narrow frequency band at $\nu \sim 28.5$ GHz. Because their measurements are effectively at a single frequency they are unable to constrain both a central Comptonization and a peculiar velocity from their data alone. Instead, the SZ results quoted by Reese et al. (2002) give the central intensity of each cluster in units of thermodynamic temperature. The measured difference temperature, $\Delta T$, is then a sum of thermal and kinematic components with

$$\Delta T = y_0 T_{\rm CMB} \frac{(e^x - 1)^2}{x^4 e^x} \frac{m_e c^2}{k T_e} \left[ \Psi(x, T_e) - \frac{v_p}{c} h(x, T_e) \right] \tag{19}$$

where $\Psi(x, T_e)$ and $h(x, T_e)$ are fully specified in Benson et al. (2003) and include relativistic corrections to their frequency dependence based on the calculations of Rephaeli (1995) and Nozawa et al. (1998) respectively.

In order to compare the BIMA and OVRO measurements to ours we want to fit a central Comptonization to the temperature decrement given in Reese et al. (2002). The observations described in Reese et al. (2002) were taken in two different receiver configurations with central observing frequencies of $\nu = 28.5$ and 30.0 GHz respectively. Reese et al. (2002) does not systematically note which sets of data correspond to which observing frequency. Because we are nearly in the Rayleigh-Jeans region of the spectrum, the calculated central Comptonization for a typical cluster varies by $< 1\%$ if we assume a central observing frequency between 28.5 and 30.0 GHz. For simplicity, we therefore assume all observations in Reese et al. (2002) were taken at a central observing frequency of $\nu = 28.5$ GHz with a Gaussian envelope 0.5 GHz in width. We can then calculate a central Comptonization derived from the published central decrements in Reese et al. (2002) in a way exactly analogous to the method in section 4.1, which was used to analyze the SuZIE 145 GHz data. From equation 19, we calculate a two-dimensional $\chi^2(v_p, y_0)$ over an appropriate range of parameter space for peculiar velocity and central Comptonization. Under the assumption of Gaussian errors on $\Delta T$, we calculate a likelihood, $L(v_p, y_0) \propto \exp(-\chi^2(v_p, y_0)/2)$. We multiply $L(v_p, y_0)$ by a Gaussian prior on the peculiar velocity, where $L(v_p) \propto \exp(-v_p^2/2\sigma_v^2)$, with $\sigma_v = 0, 500$, and 2000 km s$^{-1}$ as our three cases. We then marginalize the resultant likelihood over peculiar velocity to calculate the best-fit Comptonization and 68% confidence region for the three cases of $\sigma_v$ and give these results in Table 12

In general the main effect of increasing the width of the Gaussian prior on the peculiar velocity is to expand the corresponding confidence region for the central Comptonization. For each cluster the BIMA and OVRO best-fit central Comptonization changes negligibly between the different priors, however the width of the confidence region expands by a factor of $\approx 2 - 3$ between an exactly zero peculiar velocity and $\sigma_v = 2000\,\mathrm{km\,s^{-1}}$.

### 5.2. Comparing SuZIE to BIMA/OVRO

We can compare the central Comptonization results calculated from BIMA/OVRO to the central Comptonization calculated from both the SuZIE multi-frequency data and the SuZIE 145 GHZ data. The SuZIE 145 GHz data gives better constraints on the central Comptonization than the multi-frequency results, for reasons discussed in section 4.1, however both comparisons are useful because they are sensitive to different systematics. For example, the SuZIE multi-frequency results may be more appropriate if clusters have larger peculiar velocities than expected, conversely the SuZIE 145 GHz data would be more appropriate if sub-millimeter point sources bias the higher frequency channels.

To facilitate comparison to the BIMA/OVRO results, we re-analyze the multi-frequency SuZIE results from section 3.5 using the same method used to analyze the BIMA/OVRO results as described in the previous section. In Table 12 we give the best-fit Comptonization and 68% confidence region derived from the multi-frequency SuZIE results assuming three different priors on the peculiar velocity with Gaussian widths of $\sigma_v = 0, 500$, and 2000 km s$^{-1}$. We note that we are considering a broader range of priors on the peculiar velocity on the SuZIE multi-frequency results versus the SuZIE 145 GHz results. We do this because the multi-frequency results already constrain the peculiar velocity to some degree and therefore should be more appropriate if we are considering a larger range of possible peculiar velocities.

Comparing the results of Table 12, the SuZIE derived central Comptonizations are higher than the results from BIMA and OVRO for all the clusters except Cl0016. For the case of $\sigma_v = 500$ km s$^{-1}$, the clusters A697, A773, RXJ147, A1835, and A2261 all have significantly higher Comptonizations as measured by SuZIE. Even for the case of $\sigma_v = 2000$ km s$^{-1}$, the clusters A1835 and A2261 are still significantly inconsistent between the two data sets.

If instead we compare the central Comptonizations calculated from the SuZIE 145 GHz data in section 4.1 to the BIMA and OVRO results, SuZIE continues to measure a higher central Comptonization for most clusters. Figure 5 plots the central Comptonization calculated from the SuZIE 145 GHz data, calculated in section 4.1, to the central Comptonization calculated from the BIMA and OVRO measurements, where we have assumed $\sigma_v = 500$ km s$^{-1}$ for both calculations. Again the SuZIE derived central Comptonizations are systematically higher than the OVRO/BIMA results, particularly in cooling flow clusters. On average, the SuZIE calculated central Comptonizations are $\sim 12\%$ higher in the non-cooling flow clusters, and $\sim 60\%$ higher in the cooling flow clusters.

This discrepancy is equivalent to the statement that SuZIE is measuring a systematically higher SZ flux than expected for the spherical isothermal beta model normalized to the central Comptonization given in Reese et al. (2002). This suggests that the SuZIE measurement is either inconsistent with this central Comptonization, and/or the IC gas model. It was shown in section 4.1, that the central Comptonization derived by SuZIE is very sensitive to the assumed IC gas model. Given that SuZIE is sensitive to different spatial scales than OVRO or BIMA, it is possible that the SuZIE measurements be consistent with the OVRO and BIMA measurements and still derive a different central Comptonization if the Beta model does not fit the IC gas distribution well. This discrepancy will be investigated further in a future paper.

## 6. SZ Scaling Relations

Self-similar models of cluster formation, which include only gravity and shock heating, predict scaling relations between the electron temperature, integrated SZ flux, and central Comptonization, (see Kaiser 1986; Navarro et al. 1995; da Silva et al. 2003, for example). In the self-similar model the mass and temperature of a cluster are related by $ME(z) \propto T^{3/2}$, where $E(z)^2 \equiv \Omega_M(1+z)^3 + (1-\Omega_M-\Omega_\Lambda)(1+z)^2 + \Omega_\Lambda$. The factor of $E(z)$ arises from the assumption that the cluster density scales with the mean density of the Universe. Following da Silva et al. (2003), the mass-temperature scaling relation can be used to relate the SZ flux, $S$, to the temperature

$$S d_A(z)^2 E(z) \propto T^{5/2} \tag{20}$$

where $d_A(z)$ is the angular diameter distance to the cluster. The factor of $d_A(z)^2$ accounts for the apparent angular size of the cluster, which changes with the cluster's redshift. The scaling of the central Comptonization with the temperature can be derived through its relation to the integrated SZ flux

$$S = \int \Delta I d\Omega \propto y_0 \int d\Omega \propto \frac{y_0}{d_A^2} \int dA \tag{21}$$

where $dA$ corresponds to a physical radius such that $\int dA = \pi r^2$, where $r$ is the radius of the cluster. The radius of the cluster can be related to the cluster mass, $M$, and the critical density of the universe, $\rho_{\rm crit}$, by equation 16, such that $r^3 \propto M/\rho_{\rm crit} \propto T^{3/2}/E(z)^3$, where we have used the mass-temperature relation, $ME(z) \propto T^{3/2}$. Combining this result with the SZ flux-temperature scaling relation, and the definition of the central Comptonization above, we arrive at

$$\frac{y_0}{E(z)} \propto T^{3/2} \tag{22}$$

as the expected scaling between the central Comptonization and the temperature of the cluster. The published temperatures that we use are spectral temperatures derived from fits to X-ray spectra. As previously mentioned, simulations by Mathiesen & Evrard (2001) predict that temperatures derived from spectral fits to X-ray data would be $\sim$ 1-3keV less than the mass weighted temperature. Mathiesen & Evrard (2001) calculated the effect of using the spectral temperature in place of the mass-weighted temperature in the mass-temperature scaling relation and found $ME(z) \propto T^{1.6}$. Because we are using spectral temperatures when calculating our scaling relations, we expect equations 20 and 22 to be proportionally steepened.

The predicted slopes and offsets of the above scaling relations also change from the presence of other cooling and heating processes. Heat input, through sources such as radiative cooling or pre-heating, steepens the slope of the mass-temperature,X-ray luminosity-temperature, and SZ flux-temperature scaling relations (see Verde et al. 2002; da Silva et al. 2003, for example). The steepening of the X-ray luminosity-temperature and mass-temperature relations have been observed by several authors using X-ray measurements (see Markevitch 1998; Finoguenov et al. 2001, for example). In particular, Finoguenov et al. (2001) found that $M \propto T_X^{1.78^{+0.10}_{-0.09}}$ (68%) from X-ray observations of relatively nearby ($z \lesssim 0.1$) clusters, which is significantly steeper than the self-similar predicted slope of 1.5. Little work has been done to measure SZ scaling relations due to the scarcity of SZ measurements. Cooray (1999) and McCarthy et al. (2003) have compiled SZ measurements from the literature, but concentrated almost entirely on relations using the central decrement, which as we have shown could be susceptible to significant systematic uncertainties. No measurements exist of an integrated SZ flux-temperature relation. This study is also the first which use results entirely from one instrument to construct SZ scaling relations.

### 6.1. Definition of the Fit

To fit the following relations we perform a linear least squares regression in log space. Uncertainties for an arbitrary variable $X$ are transformed into log space by the relation $\sigma_{log(X)} = (X^+ - X^-)/(2X) \times \log(e)$ where $X^+$ and $X^-$ are the positive and negative errors, respectively, to the variable $X$. We perform a linear least squares regression to the generic relation $\log(Y) = A + B\log(X)$ where we determine the best-fit values of $A$ and $B$ by minimizing our $\chi^2$ statistic which we define as

$$\chi^2 = \sum_{i=1}^{N} \frac{(\log(Y_i) - B\log(X_i) - A)^2}{\sigma^2_{\log(Y_i)} + (B\sigma_{\log(X_i)})^2} \tag{23}$$

where $\sigma_{\log(X_i)}$ and $\sigma_{\log(Y_i)}$ are the uncertainties to $X_i$ and $Y_i$, respectively, transformed into log space, as defined above, for the $i$th cluster. The uncertainties on $A$ and $B$, $\sigma_A$ and $\sigma_B$, are defined in a standard way using a general definition from a linear least squares fit (see

Press et al. 1992, for example).

### 6.2. $S(r_{2500})d_A^2E(z)$–$T_X$

In this section we construct an integrated SZ flux, $S(r_{2500})$, versus X-ray temperature, $T_X$, scaling relation. The values we use for $S(r_{2500})$, $E(z)$, $T_X$, and $d_A$ are given in Table 9. Where relevant, the data in Table 9 assumes the cooling flow corrected temperature. According to the method described in section 6.1, we fit a line to $\log[S(r_{2500})d_A(z)^2E(z)]$ versus $\log[T_X]$ whose best-fit relationship is

$$\log\left[\frac{S(r_{2500})d_A^2E(z)}{\mathrm{JyMpc}^2}\right] = (2.76 \pm 0.41) + (2.21 \pm 0.41)\log\left[\frac{T_X}{\mathrm{keV}}\right] \tag{24}$$

where the error bars correspond to the 68% confidence region for both the offset and slope. The $\chi^2$ to the fit is 6.52 for 13 degrees of freedom. This low $\chi^2$ implies that we are not seeing any sources of intrinsic scatter in the relation, and are currently limited by measurement uncertainty. Figure 6 plots $S(r_{2500})d_A(z)^2E(z)$ versus $T_X$ for the entire 15 cluster sample with the best-fit line from equation 24 over-plotted. The best-fit slope is slightly less than the expected self similar slope of 2.5, see equation 20, however it is well within the 68% confidence region. X-ray measurements suggest a steeper mass-temperature relation which would also imply a steeper slope approximately between 2.7-2.9 for the integrated SZ flux-temperature relation. Our results suggest a smaller slope, however they lack the sensitivity to say anything significant regarding this difference.

It is also of interest to consider any systematic difference between the cooling flow and non-cooling flow sub-samples. In Table 13 we show the results of the fits to equation 24 if we consider the cooling flow and non-cooling flow sub-samples separately. The best-fit lines for the two sub-samples are nearly identical, and almost unchanged to the best-fit line for the entire sample. This suggests either that the presence of cooling flows make a negligible correction to the SZ flux-temperature scaling relation, or that the temperature we are using have accurately corrected for the presence of the cooling flows. We can test which is the case by re-calculating the scaling relation using the cooling-flow uncorrected temperatures. We do this by re-calculating $S(r_{2500})$, as prescribed in section 4.2, instead assuming the X-ray emission weighted temperatures in Table 2, which do not account for the cooling flow. The right panel of Figure 6 re-plots $S(r_{2500})d_A(z)^2E(z)$ versus $T_X$ using the re-calculated values of $S(r_{2500})$ with these different temperatures. Comparing the left to the right panel of Figure 6, only the points for the cooling flow clusters are changed, with the cooling flow clusters in the right panel having generally lower electron temperatures because they do not account for their cool cooling core in their determination of the electron temperature.

In Table 13, we give the new best-fit lines for the entire 15 cluster sample, and then the cooling flow and non-cooling flow sub-samples separately. The best-fit line which describes the cooling flow clusters is significantly changed between the cooling flow un-corrected and cooling flow corrected temperatures. This suggests that the presence of the cooling flow needs to accounted for in calculating the electron temperature in order to accurately measure the $S(r_{2500})d_A^2E(z)$–$T_X$ scaling relation.

### 6.2.1. *Measuring the Evolution of the $S(r_{2500})d_A^2E(z)$–$T_X$ Relation*

The temperature of the intra-cluster gas is expected to scale with $E(z)$ based on the assumption that the density of the gas scales with the mean density of the universe. As was mentioned at the beginning of this section, this effect causes a redshift evolution in the mass-temperature relation such that $ME(z) \propto T^{3/2}$. The redshift evolution of this relation was constrained by X-ray observations in Vikhlinin (2002). A similar redshift evolution is expected in the SZ flux-temperature relation, such that $Sd_A(z)^2E(z) \propto T^{5/2}$, as a direct consequence of the redshift evolution in the mass-temperature relation. However, other non-gravitational physics could affect this predicted redshift evolution.

Recently da Silva et al. (2003) used numerical simulations to study the evolution of the integrated SZ flux versus X-ray temperature relation when including other non-gravitational effects in clusters, such as from radiative cooling or pre-heating of the intra-cluster gas. They parameterized an arbitrary evolution by assuming that the temperature of the intra-cluster gas scaled like $E(z)^\gamma$ and then fit for $\gamma$ using simulated clusters which included either radiative cooling or pre-heating. They calculated $\gamma = 1.49$ in their simulations which included radiative cooling and $\gamma = 1.22$ in their simulations which included pre-heating instead. To fit our data we adopt a similar approach to da Silva et al. (2003) and fit the relation

$$\log\left[\frac{S(r_{2500})d_A^2E(z)^\gamma}{\mathrm{JyMpc^2}}\right] = A + B\log\left[\frac{T_X}{\mathrm{keV}}\right] \tag{25}$$

while allowing $\gamma$ to be a free-parameter, where we have assumed the cooling-flow corrected electron temperature, for the cooling flow clusters, in our calculation of $S(r_{2500})$ and $T_X$. We calculate the $\chi^2$ of the fit to equation 25 for a range of $\gamma$, letting the offset and slope, $A$ and $B$, go to their best-fit values for each value of $\gamma$. We then calculate our best-fit value of $\gamma$ and its associated confidence regions using a maximum likelihood estimator, where $L(\gamma) \propto \exp(-\chi^2(\gamma)/2)$. Doing this we calculate $\gamma = 1.16^{+0.84+1.28}_{-0.71-1.14}$, where the uncertainties correspond to the 68% confidence region followed by the 90% confidence region. Our results do not have sufficient sensitivity to significantly favor either of the models of da Silva et al. (2003). However, we can rule out at $\sim 90\%$ confidence zero evolution to the integrated SZ flux-temperature relation; this is the first constraint of any kind on the redshift evolution of this relation. Furthermore, the redshift evolution we observe is consistent with standard theories of cluster formation ($\gamma = 1$), and offers indirect evidence regarding the redshift evolution of the mass-temperature relation.

### 6.3. $y_0/E(z)$–$T_X$

In this section we construct a central Comptonization, $y_0$, versus X-ray temperature, $T_X$, scaling relation. We showed in section 4.3 that the central Comptonization had a significant systematic uncertainty due to the modelling of the IC gas distribution. Therefore we would expect this systematic uncertainty to make any scaling relation involving the central Comptonization suspect at best. However, it may be interesting to see how this systematic uncertainty manifests itself in a $y_0/E(z)$–$T_X$ scaling relation.

To construct a $y_0/E(z)$–$T_X$ scaling relation we use the central Comptonizations calculated in section 4.1 and the X-ray temperatures, $T_X$, given in Table 9. Where relevant, the data in Table 9 assumes the cooling flow corrected temperature. We fit a line to $\log(y_0/E(z))$ versus $\log(T_X/\mathrm{keV})$, according to the method described in section 6.1, whose best-fit relationship is

$$\log\left[\frac{y_0}{E(z)}\right] = (-2.35 \pm 0.57) + (2.90 \pm 0.57)\log\left[\frac{T_X}{\mathrm{keV}}\right] \tag{26}$$

where the error bars correspond to the 68% confidence region for both the offset and slope. The $\chi^2$ to the fit is 38.0 for 13 degrees of freedom, with the $\chi^2$ dominated by the contribution from A1835. Figure 7 plots $y_0/E(z)$ versus $T_X$ for the entire 15 cluster sample with the best-fit line from equation 26 over-plotted. To check the effect of A1835 on the overall fit, we refit equation 26 excluding A1835, with these results given in Table 14. Excluding A1835 negligibly changes the best-fit values for the slope and offset while reducing the $\chi^2$ to 15.0 for 12 degrees of freedom. This seems to indicate our fit of the $y_0$–$T_X$ scaling relation is reasonable, however the best-fit slope in equation 26 is inconsistent with the self-similar prediction of 1.5.

If we consider the cooling flow and non-cooling flow clusters separately there is a significant systematic difference between them. In Table 14 we show the results of the fits to equation 26 if we consider the cooling flow and non-cooling flow sub-samples separately. The best-fit line to the cooling flow clusters actually favors a negative slope but is clearly poorly constrained. If we exclude A1835 from the cooling flow sample, and refit the remaining clusters, we calculate a best-fit line which is consistent with the non-cooling flow sub-sample, however the constraints on the slope are very poor. The best-fit line to the non-cooling flow sub-sample has a slope marginally consistent with the self-similar prediction. From Figure 7 it is clear that the cooling flow sub-sample is not well fit by a line. This is not surprising considering that in section 4.1 we showed that the central Comptonization has a large systematic dependence on the assumed spatial gas distribution for cooling flow clusters. The non-cooling flow sub-sample visibly gives a better fit to a line than the cooling flow sub-sample, however it is difficult to ascertain the degree of systematic uncertainty in this relation.

## 7. Conclusions

We report new measurements of the SZ effect from clusters of galaxies in three frequency bands. We use the multi-frequency measurements to measure the SZ spectrum and the central Comptonization in each cluster. We combine these new measurements with previous cluster observations to construct a sample of 15 clusters of galaxies detected with the SuZIE experiment. For the entire set of clusters we use the 145 GHz frequency band to calculate a central Comptonization, $y_0$, and an integrated SZ flux, $S(r_{2500})$.

We find that the calculated central Comptonization is much more sensitive to the assumed spatial model for the intra-cluster gas than the calculated integrated SZ flux. The calculated central decrement depends significantly on the assumed spatial distribution of the intra-cluster (IC) gas. For the case of A1835 the calculated central Comptonization can vary by a factor of two depending on which of two different published IC gas models is assumed. This result is not surprising considering the fact that SuZIE II does not significantly resolve any of the observed clusters. This effect causes the calculated central Comptonization to have a particularly large systematic uncertainty in cooling flow clusters because of their large cooling core which makes the standard Beta model an inadequate fit to the spatial distribution of the gas. However, our measurements of the integrated SZ flux, $S(r_{2500})$, negligibly depend on the assumed spatial distribution of the IC gas because $r_{2500}$ is well-matched to our beam-size for most of the observed clusters.

Ten of the clusters in our sample overlap with published measurements from the BIMA and OVRO interferometers. For these clusters, we compare the calculated central Comptonization from BIMA and OVRO to those from SuZIE and find that the SuZIE calculated central Comptonizations are generally higher, significantly so in the cooling flow clusters. If we compare the SuZIE 145 GHz results to the BIMA and OVRO results, SuZIE measures a central Comptonization $\sim 12\%$ higher in the non-cooling flow clusters, and $\sim 60\%$ higher in the cooling flow clusters. We attribute this difference to the large systematic uncertainty in the calculated central Comptonization from the assumed intra-cluster gas model which, as expected, is more pronounced in our cooling flow sub-sample.

We use the central Comptonization and integrated SZ flux results from the SuZIE 145 GHz data to construct SZ scaling relations with the X-ray temperature, $T_X$. We construct a $y_0$–$T_X$ scaling relation and find a slope significantly different than what is expected for self-similar clusters. However, we believe that this result is questionable because of the large systematic uncertainty in the central Comptonization. This conclusion is supported by the significantly discrepant scaling relations derived for the cooling flow and non-cooling flow sub-samples. For the $S(r_{2500})$–$T_X$ scaling relation we find a slope which is consistent with the expectation for self-similar clusters. In constructing this relation, we find that using X-ray temperatures which do not account for the presence of the cooling flow significantly biases the best-fit relation. We detect a redshift evolution of the $S(r_{2500})$–$T_X$ scaling relation consistent with standard cluster formation theory for which the density of the cluster scales with the mean density of the universe. If we assume that the X-ray temperature is a good indicator of the mass of the cluster, as suggested from X-ray measurements, our results imply that the the integrated SZ flux will be a good indicator of the cluster mass as well, a promising result for future SZ cluster surveys.

We thank Jim Bartlett, Gilbert Holder, and Phil Marshall for many useful discussions. The SuZIE program is supported by a National Science Foundation grant AST-9970797, NASA grant NAG5-12973, and a Stanford Terman Fellowship awarded to SEC. This work was partially carried out at the Infrared Processing and Analysis Center and the Jet Propulsion Laboratory of the California Institute of Technology, under a contract with the National Aeronautics and Space Administration. We would like to thank the CSO staff for their assistance with SuZIE observations. The CSO is operated by the Caltech Submillimeter Observatory under contract from the National Science Foundation.

## REFERENCES


Allen, S.W., & Fabian, A.C., 1998, MNRAS, 297, L57

Allen, S.W., 2000, MNRAS, 315, 269

Allen, S.W., Ettori, S., & Fabian, A.C. 2001, MNRAS, 324, 877

Benson, B.A., Church, S.E., Ade, P.A.R., Bock, J.J., Ganga, K.M., Hinderks, J.R., Mauskopf, P.D., Philhour, B., Runyan, M.C., & Thompson, K.L. 2003, ApJ, 592, 674

Carlstrom, J. E., Holder, G.P., & Reese, E.D. 2002, ARA&A, 40 in press

Cavaliere, A. & Fusco-Femiano, R. 1976, A&A, 49, 137

Cavaliere, A. & Fusco-Femiano, R. 1978, A&A, 70, 677

Church, S.E., & Benson, B.A., in prep

Cooray, A. 1999, MNRAS, 307, 841

da Silva, A.C., Kay, S.T., Liddle, A.R., & Thomas, P.A., 2003, astro-ph/0308074

David, L. P., Slyz, A., Jones, C., Forman, W., & Vrtilek, S. D. 1993, ApJ, 412, 479

Donahue, M., 1996, ApJ, 468, 79

Dupke, R. A. & Bergman, J. N. 2002, ApJ, 575, 634

Ebeling, H., Voges, W., Bohringer, H., Edge, A. C., Huchra, J. P., & Briel, U. G. 1996a, MNRAS, 281, 799

Ebeling, H., Voges, W., Bohringer, H., Edge, A. C., Huchra, J. P., & Briel, U. G. 1996b, MNRAS, 283, 1103

Ebeling, H., Edge, A. C., Bohringer, H., Allen, S. W., Crawford, C. S., Fabian, A. C., Voges, W., & Huchra, J. P. 1998, MNRAS, 301, 881

Ettori, S., & Fabian, A.C., MNRAS, 305, 834

Evrard, A.E., Metzler, C.A., & Navarro, J.F. 1996, ApJ, 469, 494

Finoguenov, A., Reiprich, T.H., & Bohringer, H. 2001, A&A, 368, 749

Gioia, I. M. & Luppino, G. A. 1994, ApJS, 94, 583

Goldin, A.B., Kowitt, M.S., Cheng, E.S., Cottingham, D.A., Fixsen, D.J., Inman, C.A., Meyer, S.S., Puchalla, J.L., Ruhl, J.E., and Silverberg, R.F. 1997, ApJ, 488, L161

Gramann, M., Bahcall, N. A., Cen, R., & Gott, J. R. 1995, ApJ, 441, 449

Griffin, M.J., & Orton, G.S. 1993, Icarus, 105, 537

Haiman, Z., Mohr, J.J., & Holder, G.P., 2001, ApJ, 553, 545

Holder, G.P., Haiman, Z., & Mohr, J.J., 2001, ApJ, L111

Holzapfel, W.L., Arnaud, M., Ade, P.A.R., Church, S.E., Fischer, M.L., Mauskopf, P.D., Rephaeli, Y., Wilbanks, T.M., and Lange, A.E. 1997a, ApJ, 480, 449

Holzapfel, W.L., Ade, P.A.R., Church, S.E., Mauskopf, P.D., Rephaeli, Y., Wilbanks, T.M., and Lange, A.E. 1997b, ApJ, 481, 35

Hughes, J.P., & Birkinshaw, M., 1998, ApJ, 501, 1

Kaiser, N., 1986, MNRAS, 222, 323

Majerowicz, S., Neumann, D.M., & Reiprich, T.H. 2002, A&A, 394, 77

Markevitch, M., Mushotzky, R., Inoue, H., Yamashita, K., Furuzawa, A.,& Tawara, Y. 1996, ApJ, 456, 437

Markevitch, M. 1998, ApJ, 504, 27

Markevitch, M., Gonzalez, A. H., Clowe., D., Vikhlinin, A., David, L., Forman, W., Jones, C., Murray, S., & Tucker, W. 2003, ApJ, submitted, astroph/0309303

Mathiesen, B.F. & Evrard, A.E. 2001, ApJ, 546, 100

Mauskopf, P.D., Bock, J.J., Del Castillo, H., Holzapfel, W.L., & Lange, A.E., 1997, Applied Optics, Vol. 36, No. 4, 765

McCarthy, I. G., Holder, G. P., Babul, A., & Balogh, M. L., 2003, ApJ, 591, 526

Mohr, J.J., Reese, E.D., Ellingson, E., Lewis, A.D., & Evrard, A.D. 2000, ApJ, 544, 109

Navarro, J.F., Frenk, C.S., & White, S.D.M., 1995, MNRAS, 274, 720

Nozawa, S., Itoh, N., & Kohyama, Y., 1998, ApJ, 508, 17

Peterson, J.R., Paerels, F.B.S., Kaastra, J.S., Arnaud, M., Reiprich, T.H., Fabian, A.C., Mushotzky, R.F., Jernigan, J.G., & Sakelliou, I., A&A 365, L104

Press, W.H., Teukolsky, S.A., Vetterling, W.T., & Flannery, B.P., 1992, Numerical Recipes in C (New York: Cambridge Univ. Press)

Reese, E. D., Carlstrom, J. E., Joy, M., Mohr, J. J., Grego, L., & Holzapfel, W. L. 2002, ApJ, 581, 53

Reese, E. D., 2003, private communication

Rephaeli, Y. 1995, ApJ, 445, 33

Schindler, S., Hattori, M., Neumann, D.M., & Boehringer, H., 1997, A&A, 299, L9

Schulz, A.E., & White, M., 2003, ApJ, 586, 723S

Sheth, R.K, & Diaferio, A. 2001, MNRAS, 322, 901

Suhhonenko, I., & Gramann, M. 2003, MNRAS, 339, 271

Verde, L., Haiman, Z., & Spergel, D.N. 2002, ApJ, 581, 5

Vikhlinin, A., VanSpeybroeck, L., Markevitch, M., Forman, W.R., & Grego, L. 2002, ApJ, 578, L107

Wang, L., & Steinhardt, P.J. 1998, ApJ, 508, 483

This preprint was prepared with the AAS LaTeX macros v5.2.

Table 1. Summary of New SuZIE observations

| Source | z | R.A.[a] (J2000) | Decl.[a] (J2000) | Date | Total Scans | Accepted Scans | Integration Time (hours) | Ref. |
|---|---|---|---|---|---|---|---|---|
| A520 | 0.199 | 04 54 07.4 | +02 55 12.1 | Dec 02 | 462 | 435 | 14.5 | 1 |
| A545 | 0.153 | 05 32 23.3 | −11 32 09.6 | Dec 98 | 295 | 266 | 8.9 | 3 |
| A697 | 0.282 | 08 42 57.8 | +36 21 54.0 | Mar 03 | 258 | 254 | 8.5 | 1 |
| A773 | 0.217 | 09 17 52.1 | +51 43 48.0 | Mar 03 | 92 | 83 | 2.8 | 1 |
| MS1054 | 0.823 | 10 56 58.6 | −03 37 36.0 | Jan 02 | 236 | 219 | 7.0 | 4 |
| RXJ1347 | 0.451 | 13 47 31.0 | −11 45 11.0 | Mar 03 | 209 | 202 | 6.7 | 2 |
| A2204 | 0.152 | 16 32 47.0 | +05 34 33.0 | Mar 03 | 468 | 449 | 15.0 | 1 |
| A2390 | 0.232 | 21 53 36.7 | +17 41 43.7 | Dec 02 | 203 | 195 | 6.5 | 1 |

References. — (1) Ebeling et al. (1998)(2) Schindler et al. (1997)(3) Ebeling et al. (1996a)(4) Gioia & Luppino (1994)

[a]Units of RA are hours, minutes and seconds and units of declination are degrees, arcminutes and arcseconds

Table 2. IC gas temperatures and $\beta$ model parameters

| Cluster | $kT_e$[a] (keV) | $kT_e$[b] (keV) | $\beta$ | $\theta_c$ (arcsec) | CF or NCF | Ref. |
|---|---|---|---|---|---|---|
| A520 | $8.33^{+0.46}_{-0.40}$ | ··· | $0.844^{+0.040}_{-0.040}$ | $123.3^{+8.0}_{-8.0}$ | NCF | 1;2;2 |
| A545 | $5.50^{+6.2}_{-1.1}$ | ··· | $0.82^{c}$ | $115.5^{c}$ | NCF | 3;4;4 |
| A697 | $9.8^{+0.7}_{-0.7}$ | ··· | $0.540^{+0.045}_{-0.035}$ | $37.8^{+5.6}_{-4.0}$ | NCF | 2;2;2 |
| A773 | $9.29^{+0.41}_{-0.36}$ | ··· | $0.597^{+0.064}_{-0.032}$ | $45.0^{+7.0}_{-5.0}$ | NCF | 1;2;2 |
| MS1054 | $7.8^{+0.6}_{-0.6}$ | ··· | $1.39^{+0.14}_{-0.14}$ | $67.7^{c}$ | NCF | 5;5;5 |
| RXJ1347 | $9.3^{+0.7}_{-0.6}$ | $14.1^{+0.9}_{-0.9}$ | $0.604^{+0.011}_{-0.012}$ | $9.0^{+0.5}_{-0.5}$ | CF | 6;5;2;2 |
| A2204 | $7.4^{+0.30}_{-0.28}$ | $9.2^{+2.5}_{-1.1}$ | $0.66^{c}$ | $34.7^{c}$ | CF | 1;1;4;4 |
| A2390 | $10.13^{+1.22}_{-0.99}$ | $11.5^{+1.5}_{-1.6}$ | $0.67^{c}$ | $52.0^{c}$ | CF | 1;7;4;4 |
| A2261 | $8.82^{+0.37}_{-0.32}$ | $10.9^{+5.9}_{-2.2}$ | $0.516^{+0.014}_{-0.013}$ | $15.7^{+1.2}_{-1.1}$ | CF | 1;1;2;2 |
| Zw3146 | $6.41^{+0.26}_{-0.25}$ | $11.3^{+5.8}_{-2.7}$ | $0.74^{c}$ | $13.0^{c}$ | CF | 1;1;4;4 |
| A1835 | $8.21^{0.19}_{-0.17}$ | $8.2^{+0.4}_{-0.4}$ | $0.595^{+0.007}_{-0.005}$ | $12.2^{+0.6}_{-0.5}$ | CF | 1;8;2;2 |
| Cl0016 | $7.55^{+0.72}_{-0.58}$ | ··· | $0.749^{+0.024}_{-0.018}$ | $42.3^{+2.4}_{-2.0}$ | NCF | 9;2;2 |
| MS0451 | $10.4^{+1.0}_{-0.8}$ | ··· | $0.806^{+0.052}_{-0.043}$ | $34.7^{+3.9}_{-3.5}$ | NCF | 10;2;2 |
| A1689 | $9.66^{+0.22}_{-0.20}$ | $10.0^{+1.2}_{-0.8}$ | $0.609^{+0.005}_{-0.005}$ | $26.6^{+0.7}_{-0.7}$ | CF | 1;1;2;2 |
| A2163 | $12.2^{+1.1}_{-0.7}$ | ··· | $0.674^{+0.011}_{-0.008}$ | $87.5^{+2.5}_{-2.0}$ | NCF | 11;2;2 |

References. — (1) Allen & Fabian (1998), (2) Reese et al. (2002), (3) David et al. (1993), (4) Ettori & Fabian (1999), (5) Vikhlinin (2002), (6) Schindler et al. (1997), (7) Allen et al. (2001), (8) Peterson et al. (2001), (9) Hughes & Birkinshaw (1998), (10) Donahue (1996), (11) Markevitch et al. (1996)

[a]The X-ray emission weighted temperature.

[b]The cooling flow corrected X-ray emission weighted temperature.

[c]No confidence intervals were given for these parameters. It is assumed their uncertainty is comparable to the other clusters in our sample.

Table 3. Differential Atmospheric Template Factors

| Cluster | $\alpha$ | $\gamma$ |
|---|---|---|
| A520 | 0.6785 | -1.4426 |
| A545 | 0.6612 | -1.4493 |
| A697 | 0.6848 | -1.4374 |
| A773 | 0.6861 | -1.4380 |
| MS1054 | 0.7464 | -1.5391 |
| RXJ1347 | 0.6703 | -1.3773 |
| A2204 | 0.6819 | -1.4103 |
| A2390 | 0.6676 | -1.4191 |

Table 4. Cluster $RA_{offset}$ and New Multi-Frequency $y_0$ Results

| Cluster | Date | $\Delta$ RA (arcsec) | $y_0 \times 10^4$ |
|---|---|---|---|
| A520 | Dec02 | $103^{+51}_{-53}$ | $2.00^{+0.70}_{-0.73}$ |
| A697 | Mar03 | $-25^{+16}_{-17}$ | $4.79^{+1.05}_{-1.06}$ |
| A773 | Mar03 | $7^{+25}_{-27}$ | $4.23^{+2.00}_{-2.32}$ |
| RXJ1347 | Mar03 | $15^{+12}_{-12}$ | $10.65^{+2.82}_{-2.84}$ |
| A2204 | Mar03 | $3^{+21}_{-20}$ | $2.53^{+0.77}_{-0.80}$ |
| A2390 | Dec02 | $-60^{+28}_{-29}$ | $3.61^{+0.73}_{-0.74}$[a] |

[a]The central Comptonization of A2390 is calculated at $RA_{offset} = 0$ for reasons given in section 3.4

Table 5. Cluster Positions

| Cluster | Instrument | R.A.[a] (J2000) | Decl.[a] (J2000) | Ref. |
|---|---|---|---|---|
| A520 | PSPC | 04 54 07.4 | +02 55 12.1 | 1 |
| ··· | HRI | 04 54 10.1 | +02 55 27.0 | 2 |
| ··· | SuZIE | $04\ 54\ 14.3^{+3.4}_{-3.6}$ | ··· | 3 |
| ··· | ··· | ··· | ··· | ··· |
| A2390 | PSPC | 21 53 36.7 | +17 41 31.2 | 1 |
| ··· | HRI | 21 53 36.5 | +17 41 45.0 | 2 |
| ··· | SuZIE | $21\ 53\ 36.4^{+1.1}_{-1.2}$ | ··· | 4 |
| ··· | SuZIE | $21\ 53\ 32.9^{+1.7}_{-1.9}$ | ··· | 3 |

References. — (1) Ebeling et al. (1998)(2) Allen (2000)(3) This paper (4) Benson et al. (2003)

[a]Units of RA are hours, minutes and seconds and units of declination are degrees, arcminutes and arcseconds

Table 6. Summary of SuZIE Multi-Frequency Central Comptonization Results

| Cluster | Date | $y_0 \times 10^4$ | Ref. |
|---|---|---|---|
| A697 | Mar03 | $4.79^{+1.05}_{-1.06}$ | 1 |
| A773 | Mar03 | $4.23^{+2.00}_{-2.32}$ | 1 |
| RXJ1347 | Mar03 | $10.65^{+2.82}_{-2.84}$ | 1 |
| A2204 | Mar03 | $2.53^{+0.77}_{-0.80}$ | 1 |
| A520 | Dec02 | $2.00^{+0.70}_{-0.73}$ | 1 |
| A2390 | Nov00/Dec02 | $3.56^{+0.52}_{-0.51}$ | 1,2 |
| Zw3146 | Nov00 | $3.62^{+1.83}_{-2.52}$ | 2 |
| A2261 | Mar99 | $7.41^{+1.95}_{-1.98}$ | 2 |
| MS0451 | Nov96/97/00 | $2.84^{+0.52}_{-0.52}$ | 2 |
| Cl0016 | Nov96 | $3.27^{+1.45}_{-2.86}$ | 2 |
| A1835 | Apr96 | $7.66^{+1.64}_{-1.66}$ | 2 |
| A1689 | Apr94/May94 | $3.43^{+0.59}_{-0.59}$ | 3 |
| A2163 | Apr93/May93 | $3.62^{+0.48}_{-0.48}$ | 3 |

References. — (1) This paper (2) Benson et al. (2003)(3) Holzapfel et al. (1997b)

Table 7. Summary of SuZIE 145 GHz Central Comptonization Results

| Cluster | $y_0 \times 10^4$ |
| --- | --- |
| A697 | $3.55^{+0.57}_{-0.53}$ |
| A773 | $3.37^{+0.73}_{-0.66}$ |
| RXJ1347 | $12.31^{+1.89}_{-1.72}$ |
| A2204 | $2.44^{+0.43}_{-0.39}$ |
| A520 | $1.65^{+0.45}_{-0.41}$ |
| A2390 | $3.57^{+0.42}_{-0.42}$ |
| Zw3146 | $5.65^{+1.78}_{-1.58}$ |
| A2261 | $6.01^{+0.93}_{-0.81}$ |
| MS0451 | $3.12^{+0.30}_{-0.29}$ |
| Cl0016 | $2.31^{+0.93}_{-0.90}$ |
| A1835 | $6.70^{+1.40}_{-1.24}$ |
| A1689 | $5.20^{+0.58}_{-0.52}$ |
| A2163 | $3.25^{+0.40}_{-0.39}$ |
| A545[a] | $1.26^{+0.39}_{-0.30}$ |
| MS1054[a] | $3.87^{+1.19}_{-1.12}$ |

[a]These clusters were observed by SuZIE and detected at 145 GHz but lacked the sensitivity at 221 and 355 GHz to constrain their peculiar velocities.

Table 8. Re-Analysis of SuZIE I Observations

| Cluster | $kT_e$ (keV) | $\beta$ | $\theta_c$ (arcsec) | $y_0 \times 10^4$ | IC Gas Ref |
|---|---|---|---|---|---|
| A1689 | 9.66 | 0.609 | 26.6 | $5.20^{+0.58}_{-0.52}$ | 1 |
| ··· | 8.2 | 0.78 | 67.8 | $3.67^{+0.40}_{-0.38}$ | 2 |
| A2163 | 12.2 | 0.674 | 87.5 | $3.25^{+0.40}_{-0.39}$ | 1 |
| ··· | 12.4 | 0.616 | 72.0 | $3.48^{+0.42}_{-0.42}$ | 2 |

References. — (1) Reese et al. (2002) (2) Holzapfel et al. (1997b)

Table 9. Integrated SZ Flux Results

| Cluster | $z$ | $E(z)$[b] | $d_A$ (MPc) | $r_{2500}$ (kPc) | $r_{2500}$ (arcsec) | $S(r_{2500})$[a] (mJy) |
|---|---|---|---|---|---|---|
| A697 | 0.282 | 1.154 | 616 | 373 | 125 | $-245^{+45}_{-48}$ |
| A773 | 0.217 | 1.114 | 508 | 399 | 162 | $-326^{+71}_{-78}$ |
| R1347 | 0.451 | 1.271 | 833 | 448 | 111 | $-229^{+35}_{-38}$ |
| A2204 | 0.152 | 1.076 | 382 | 443 | 240 | $-266^{+50}_{-62}$ |
| A520 | 0.199 | 1.103 | 475 | 375 | 163 | $-212^{+55}_{-60}$ |
| A2390 | 0.232 | 1.123 | 534 | 465 | 179 | $-360^{+56}_{-55}$ |
| Zw3146 | 0.291 | 1.160 | 630 | 486 | 159 | $-109^{+37}_{-43}$ |
| A2261 | 0.224 | 1.118 | 520 | 413 | 164 | $-437^{+92}_{-167}$ |
| MS0451 | 0.550 | 1.348 | 926 | 390 | 86.9 | $-73.9^{+8.6}_{-8.6}$ |
| Cl0016 | 0.546 | 1.345 | 923 | 290 | 64.8 | $-47.2^{+19.3}_{-20.0}$ |
| A1835 | 0.252 | 1.135 | 568 | 379 | 138 | $-221^{+42}_{-48}$ |
| A1689 | 0.183 | 1.094 | 444 | 438 | 203 | $-459^{+50}_{-60}$ |
| A2163 | 0.202 | 1.105 | 480 | 465 | 200 | $-533^{+68}_{-74}$ |
| A545 | 0.153 | 1.077 | 384 | 321 | 172 | $-174^{+58}_{-146}$ |
| MS1054 | 0.823 | 1.587 | 1095 | 189 | 35.6 | $-30.3^{+12.8}_{-12.5}$ |

[a]The integrated SZ flux, $S(r_{2500})$, is calculated assuming the SuZIE II 145 GHz band.

[b]$E(z)^2 \equiv \Omega_M(1+z)^3 + (1-\Omega_M-\Omega_\Lambda)(1+z)^2 + \Omega_\Lambda$

[c]For all calculations where cosmology is relevant, we assume a standard $\Lambda$CDM cosmology in a flat universe with $\Omega_M = 0.3$, $\Omega_\Lambda = 0.7$, and $h = 1$.

Table 10. XMM Radial Temperature Profile[a]

| $r_{\rm inner}$ | $r_{\rm outer}$ | $kT_e$ |
|---|---|---|
| (') | | (keV) |
| 0.0 | 0.25 | $4.11 \pm 0.12$ |
| 0.25 | 0.75 | $8.03 \pm 0.39$ |
| 0.75 | 1.5 | $7.12 \pm 0.36$ |
| 1.5 | 2.25 | $7.70^{+0.87}_{-0.77}$ |
| 2.25 | 3.33 | $8.55^{+1.36}_{-1.84}$ |
| 3.33 | 6.0 | $7.72^{+3.99}_{-2.12}$ |

[a]Taken from Majerowicz et al. (2002).

Table 11. The Effect of Thermal Structure on the Results for A1835

| Analysis | Thermal Structure | $kT_e(r>6')$[a] (keV) | $y_0 \times 10^4$ | $S(r_{2500})$[b] (mJy) |
|---|---|---|---|---|
| Multi-frequency | Isothermal | 8.2 | $7.66^{+1.61}_{-1.66}$ | ... |
| | XMM | 7.6 | $7.50^{+1.60}_{-1.61}$ | ... |
| | XMM | 4.11 | $7.46^{+1.58}_{-1.59}$ | ... |
| | Isothermal | 11.5 | $7.99^{+1.70}_{-1.72}$ | ... |
| | Isothermal | 4.11 | $7.19^{+1.56}_{-1.56}$ | ... |
| ... | ... | ... | ... | ... |
| 145 GHz only | Isothermal | 8.2 | $6.70^{+1.40}_{-1.24}$ | $-221^{+42}_{-48}$ |
| | XMM | 7.6 | $6.63^{+1.46}_{-1.26}$ | $-213^{+41}_{-47}$ |
| | XMM | 4.11 | $6.71^{+1.46}_{-1.28}$ | $-215^{+41}_{-47}$ |
| | Isothermal | 11.5 | $6.87^{+1.27}_{-1.19}$ | $-226^{+39}_{-42}$ |
| | Isothermal | 4.11 | $6.29^{+2.11}_{-1.50}$ | $-204^{+49}_{-68}$ |

[a]The electron temperature at a radius greater than 6'. For the isothermal cases this temperature is equal to the temperature assumed throughout the cluster.

[b]The same definition of $r_{2500}$ is used for all models, where we have assumed $kT_e = 8.2$ keV in the calculation of $r_{2500}$.

Table 12. Central Comptonization Results with Different Priors on Peculiar Velocity.

| $\sigma_v$ (km s$^{-1}$) | $y_0 \times 10^4$ A697 | A773 | A520 | RXJ1347 | MS0451 | Cl0016 | A1835 | A2261 |
|---|---|---|---|---|---|---|---|---|
| | | | | BIMA/OVRO | | | | |
| 0 | $2.75^{+0.33}_{-0.32}$ | $2.45^{+0.30}_{-0.31}$ | $1.30^{+0.16}_{-0.20}$ | $7.65^{+0.67}_{-0.67}$ | $2.80^{+0.16}_{-0.21}$ | $2.40^{+0.19}_{-0.21}$ | $4.85^{+0.31}_{-0.31}$ | $3.30^{+0.37}_{-0.40}$ |
| 500 | $2.75^{+0.36}_{-0.34}$ | $2.45^{+0.32}_{-0.34}$ | $1.25^{+0.22}_{-0.17}$ | $7.65^{+0.77}_{-0.76}$ | $2.75^{+0.25}_{-0.19}$ | $2.40^{+0.24}_{-0.25}$ | $4.85^{+0.41}_{-0.40}$ | $3.25^{+0.45}_{-0.39}$ |
| 2000 | $2.70^{+0.71}_{-0.55}$ | $2.35^{+0.70}_{-0.49}$ | $1.20^{+0.45}_{-0.26}$ | $7.40^{+2.00}_{-1.41}$ | $2.70^{+0.62}_{-0.45}$ | $2.25^{+0.84}_{-0.48}$ | $4.65^{+1.46}_{-0.92}$ | $3.15^{+0.98}_{-0.66}$ |
| | | | | SuZIE | | | | |
| 0 | $3.92^{+0.65}_{-0.64}$ | $4.54^{+1.36}_{-1.36}$ | $1.84^{+0.59}_{-0.59}$ | $11.70^{+1.85}_{-1.85}$ | $3.30^{+0.30}_{-0.30}$ | $1.87^{+0.86}_{-0.85}$ | $8.00^{+1.14}_{-1.14}$ | $6.24^{+0.85}_{-0.84}$ |
| 500 | $4.04^{+0.77}_{-0.72}$ | $4.53^{+1.45}_{-1.40}$ | $1.88^{+0.59}_{-0.59}$ | $11.47^{+2.12}_{-2.00}$ | $3.22^{+0.35}_{-0.33}$ | $1.88^{+0.91}_{-0.87}$ | $7.97^{+1.22}_{-1.19}$ | $6.33^{+1.04}_{-0.97}$ |
| 2000 | $4.61^{+1.03}_{-1.00}$ | $4.43^{+1.85}_{-1.60}$ | $2.01^{+0.68}_{-0.67}$ | $10.87^{+2.58}_{-2.45}$ | $2.97^{+0.45}_{-0.44}$ | $2.03^{+1.80}_{-1.13}$ | $7.78^{+1.49}_{-1.41}$ | $6.99^{+1.77}_{-1.60}$ |

Table 13. Fits to $\log\left[\frac{S(r_{2500})d_A^2E(z)}{\mathrm{JyMpc^2}}\right] = A + B\log\left[\frac{T_X}{\mathrm{keV}}\right]$

| Sub-sample | $A$ | $B$ | $N$ | $\chi^2$ | $\chi^2_{\rm red}$[a] |
|---|---|---|---|---|---|
| Cooling-flow Corrected Temperatures | | | | | |
| All | $2.76 \pm 0.41$ | $2.21 \pm 0.41$ | 15 | 6.52 | 0.50 |
| Only NCF | $2.84 \pm 0.72$ | $2.13 \pm 0.71$ | 8 | 2.08 | 0.35 |
| Only CF | $2.78 \pm 0.52$ | $2.25 \pm 0.50$ | 7 | 4.47 | 0.89 |
| Cooling-flow Un-Corrected Temperatures | | | | | |
| All | $2.17 \pm 0.52$ | $2.89 \pm 0.54$ | 15 | 16.3 | 1.25 |
| Only NCF | $2.84 \pm 0.72$ | $2.13 \pm 0.71$ | 8 | 2.08 | 0.35 |
| Only CF | $1.70 \pm 0.63$ | $3.42 \pm 0.67$ | 7 | 9.15 | 1.83 |

[a] $\chi^2_{\rm red} = \chi^2/(N-2)$, where $N$ is the number of clusters in the sub-sample.

Table 14. Fits to $\log\left[\frac{y_0}{E(z)}\right] = A + B\log\left[\frac{T_X}{\mathrm{keV}}\right]$

| Sub-sample | $A$ | $B$ | $N$ | $\chi^2$ | $\chi^2_{\rm red}$[a] |
|---|---|---|---|---|---|
| All | $-2.35 \pm 0.57$ | $2.90 \pm 0.57$ | 15 | 38.0 | 2.93 |
| All(-A1835) | $-2.45 \pm 0.51$ | $2.94 \pm 0.50$ | 14 | 15.0 | 1.25 |
| Only NCF | $-0.34 \pm 0.49$ | $0.77 \pm 0.48$ | 8 | 7.1 | 1.18 |
| Only CF | $3.55 \pm 9.64$ | $-2.88 \pm 2.79$ | 7 | 55.5 | 11.1 |
| Only CF(-A1835) | $-1.11 \pm 12.8$ | $1.52 \pm 1.79$ | 6 | 32.4 | 8.1 |

[a] $\chi^2_{\rm red} = \chi^2/(N-2)$, where $N$ is the number of clusters in the sub-sample.

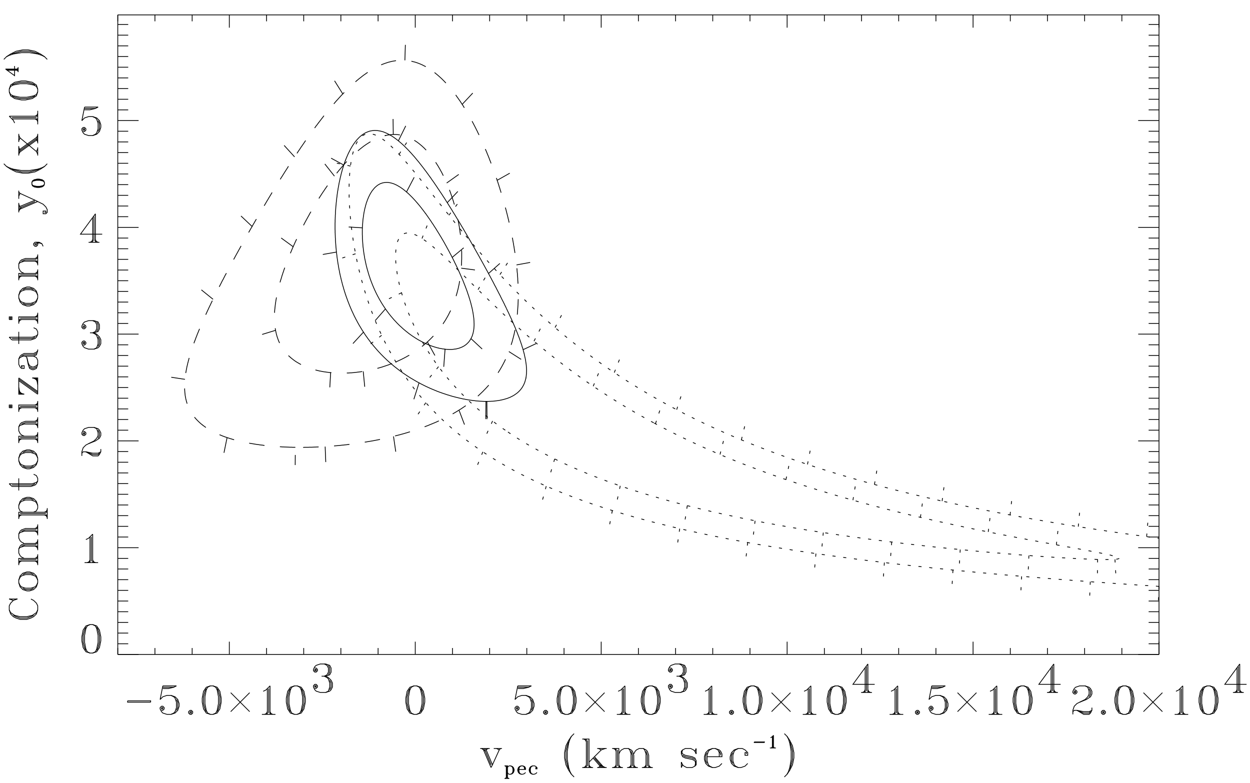


Fig. 1.— The two-dimensional likelihood of the measurements of A2390 in November 2000, December 2002, and then the combined likelihood from both observations. For each set of data the 68.3% and 95.4% confidence regions are shown for peak Comptonization and peculiar velocity. The dotted contours are from the November 2000 data, the dashed contours are from the December 2002 data, and the solid contours are from the combined likelihoods.

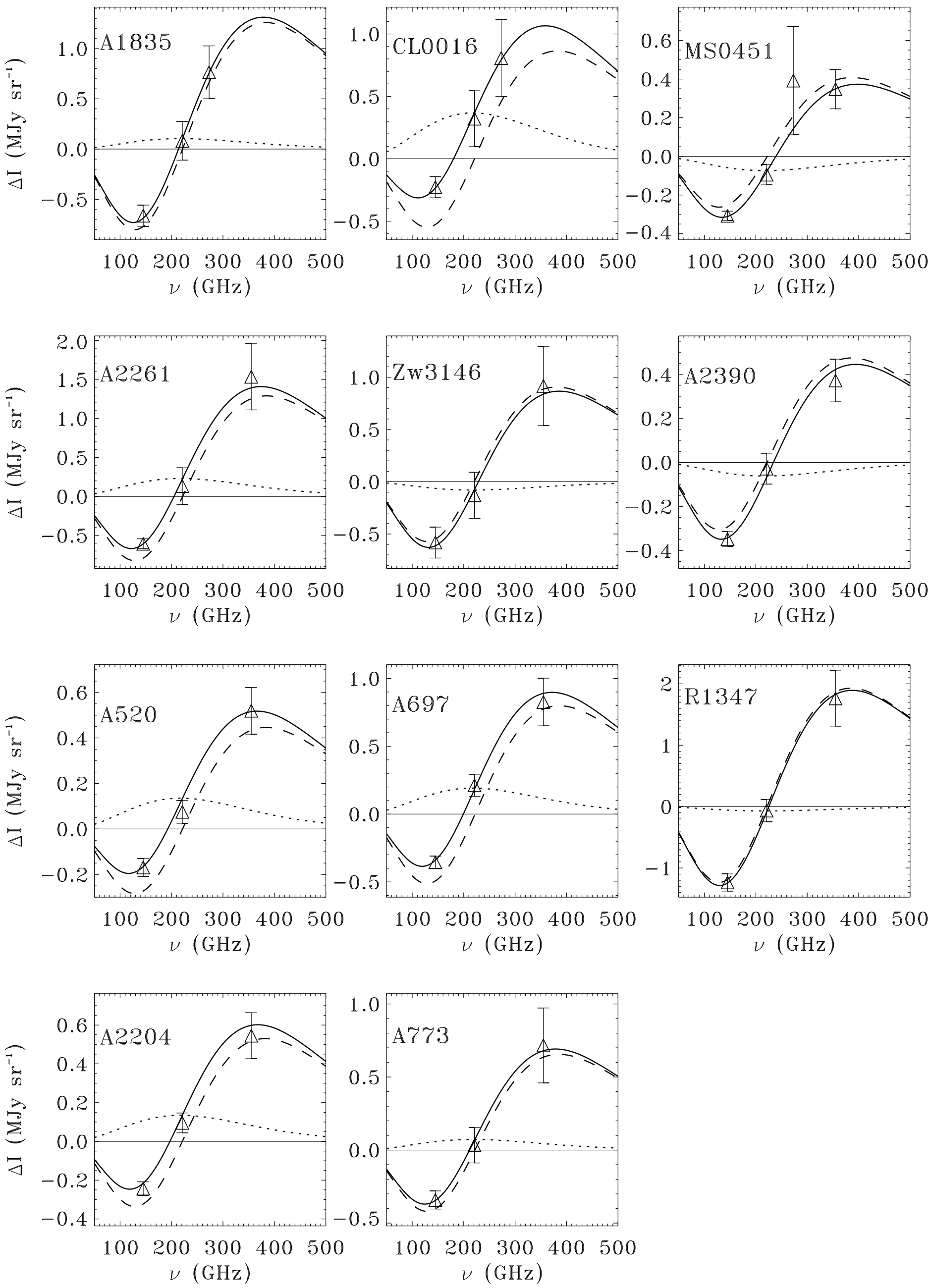


Fig. 2.— The measured SZ spectrum for each cluster observation reported in this paper and Benson et al. (2003). In each plot the solid line is the best-fit SZ model, the dashed line is the thermal component of the SZ effect and the dotted line is the kinematic component of the SZ effect.

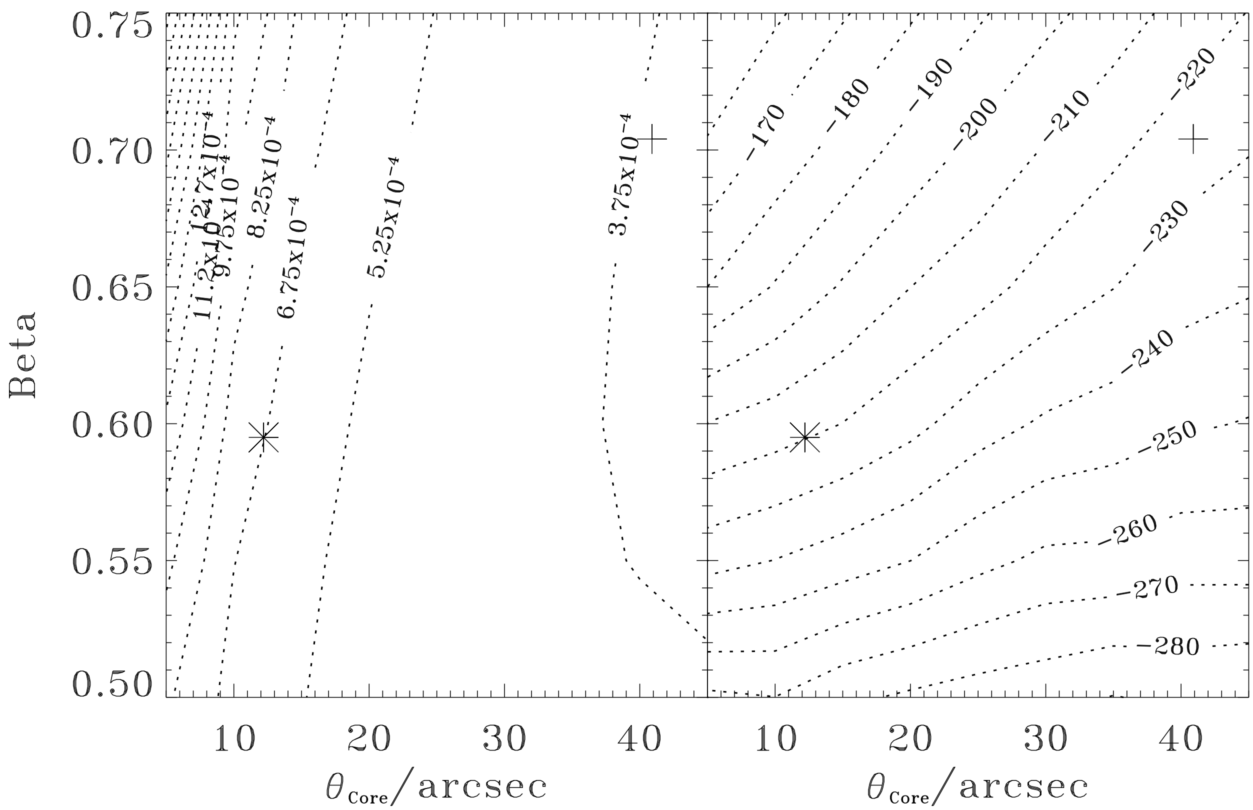


Fig. 3.— The best-fit $y_0$ and $S(r_{2500})$ calculated for A1835 using a range of Beta models. The asterisk marks where the location of the gas model given in Reese et al. (2002), and the plus sign marks the location of the Beta model given in Majerowicz et al. (2002), which fits only the outer region of the cluster. Left: The central Comptonziation of A1835, the contour levels spaced in $1.5 \times 10^{-4}$ intervals. Right: The integrated SZ flux at 145 GHz, $S(r_{2500})$, from A1835, the contour levels are spaced in 10 mJy intervals.

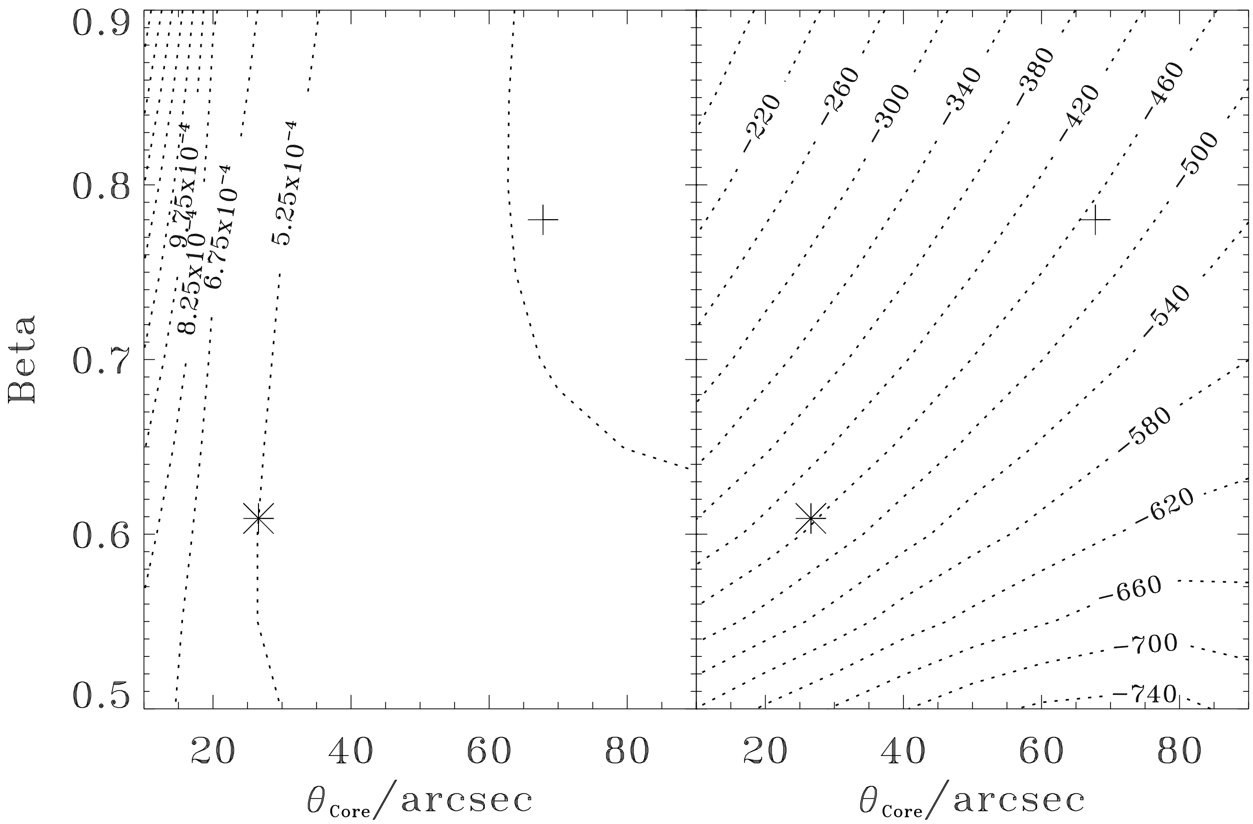


Fig. 4.— The best-fit $y_0$ and $S(r_{2500})$ calculated for A1689 using a range of Beta models. The asterisk marks where the location of the gas model given in Reese et al. (2002), and the plus sign marks the location of the Beta model given in Holzapfel et al. (1997b). Left: The central Comptonziation of A1689, the contour levels spaced in $1.5 \times 10^{-4}$ intervals. Right: The integrated SZ flux at 145 GHz, $S(r_{2500})$, from A1689, the contour levels are spaced in 40 mJy intervals.

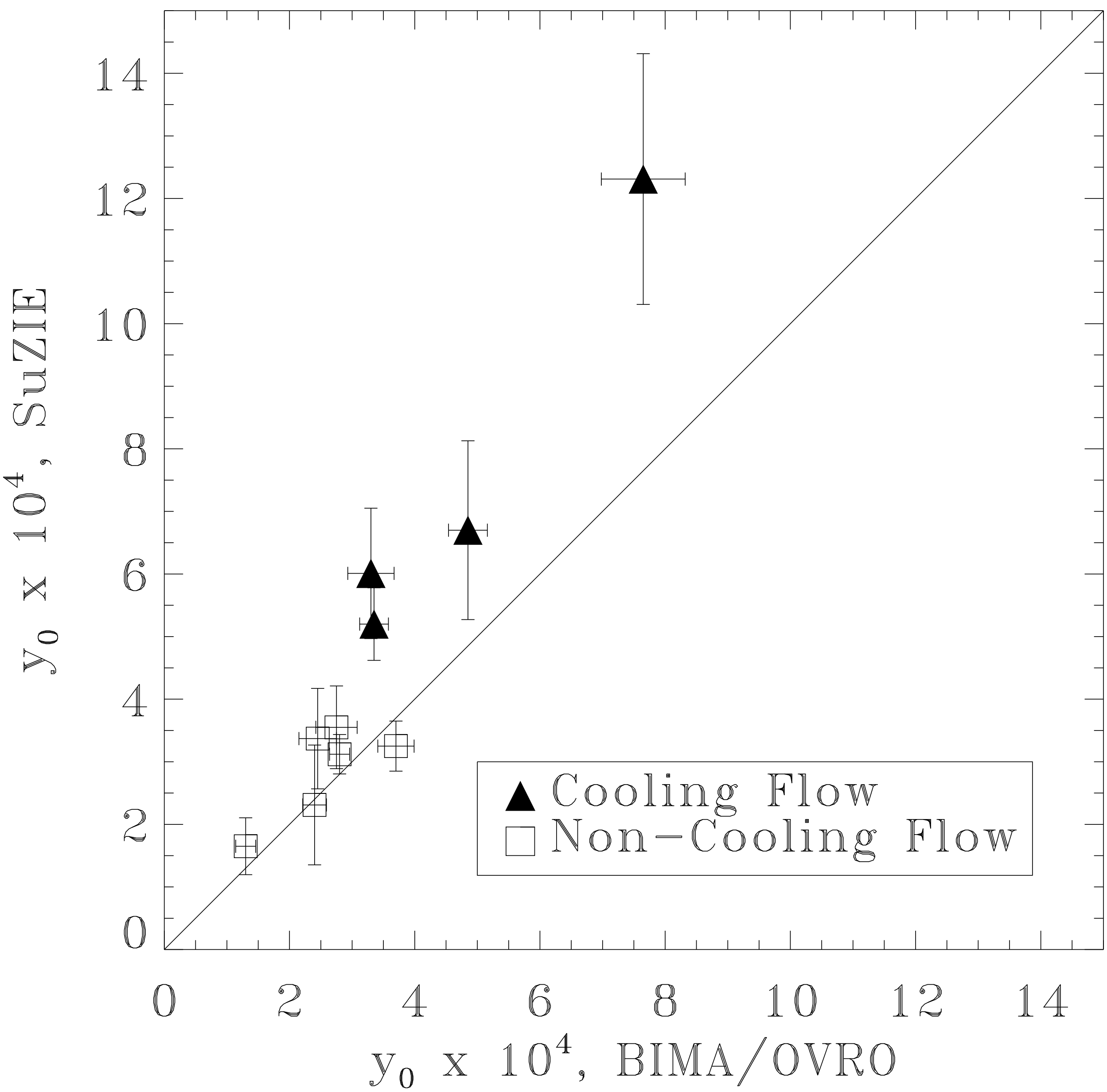


Fig. 5.— A plot of the central Comptonization measured by SuZIE versus the central Comptonization measured by the BIMA/OVRO interferometers. The SuZIE central Comptonization calculation is based on the method described in section 4.1. Both measurements assume a zero peculiar velocity with a Gaussian prior on the peculiar velocity with a width of 500 km $s^{-1}$. Clusters with cooling cores are labelled with triangles and non-cooling core clusters are labelled with squares.

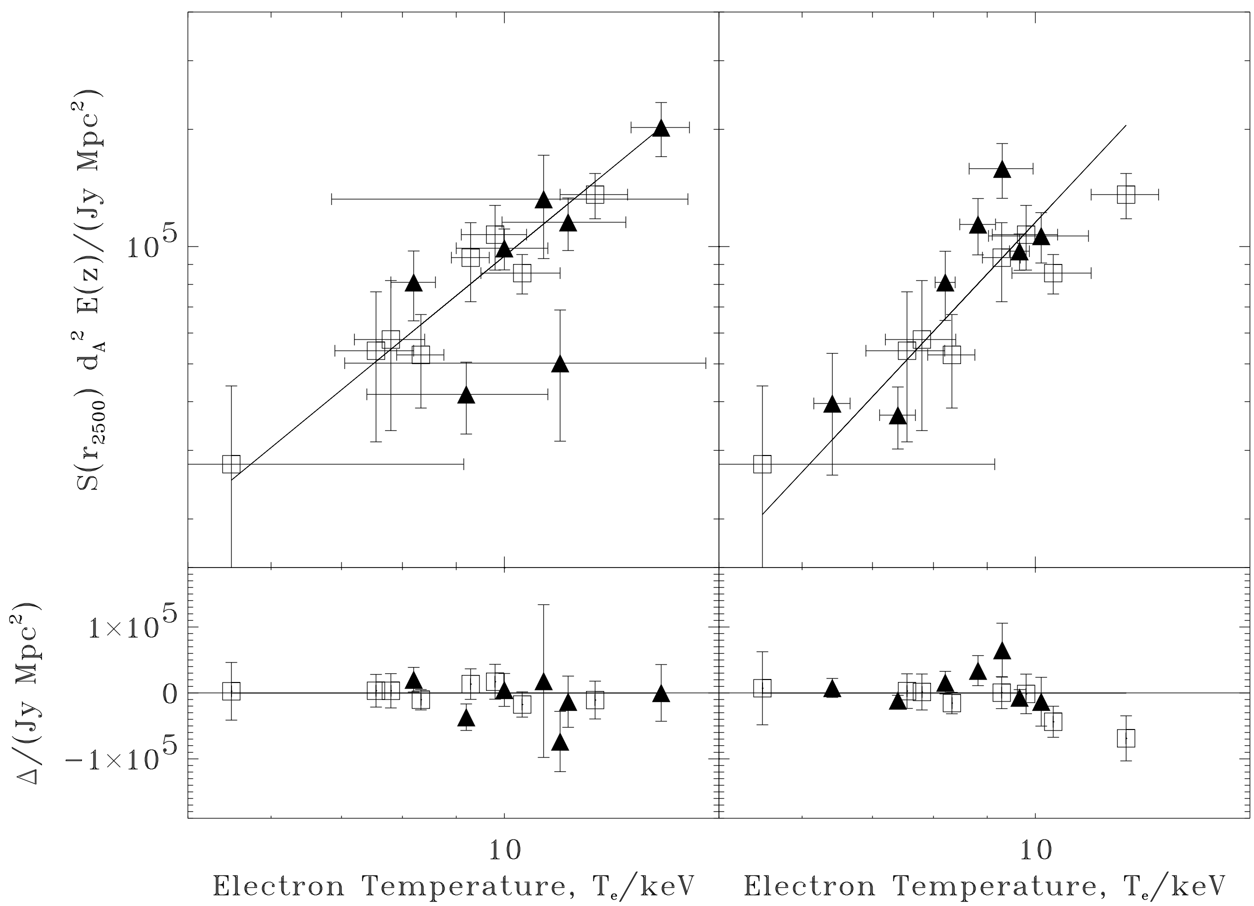


Fig. 6.— Left:(Top) A plot of the integrated SZ flux, as measured by SuZIE, versus the electron temperature. The solid line shows a power-law fit to the relation. Cooling flow clusters are plotted as triangles, and non-cooling flow clusters are plotted as squares. (Bottom) A plot of the residuals to the power-law fit. The uncertainty on electron temperature is not plotted, but instead is added in quadrature, according to equation 24, with the uncertainty to the flux density to give the uncertainty for the residual data points. Right: The same plot as on the left, except for the cooling flow clusters we use electron temperatures which do not account for the presence of the cooling flow in our calculation of $S(r_{2500})$.

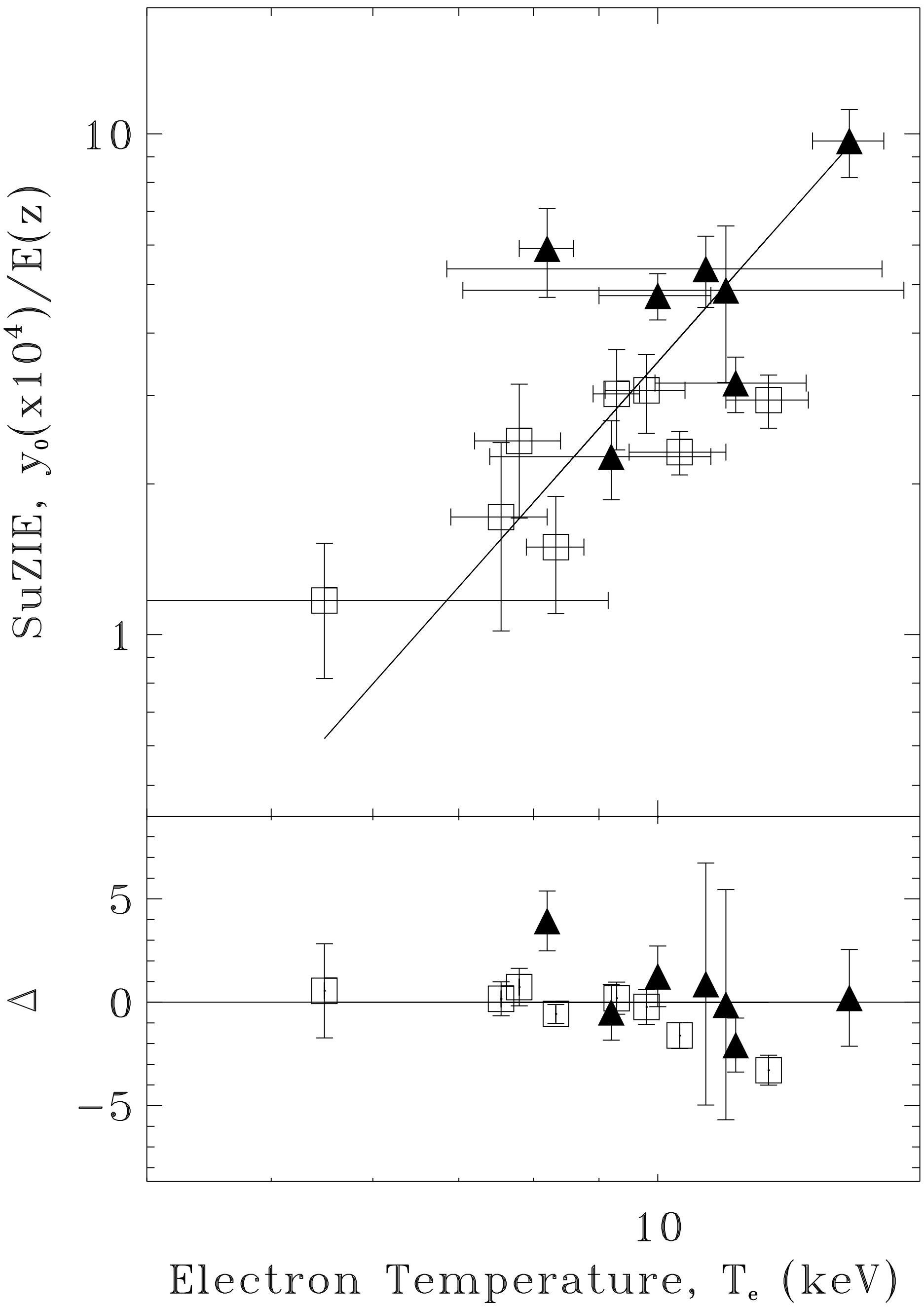


Fig. 7.— (Top) A plot of the central Comptonization, as measured by SuZIE, versus the electron temperature. The solid line shows a power-law fit to the relation. Cooling flow clusters are plotted as triangles, and non-cooling flow clusters are plotted as squares. (Bottom) A plot of the residuals to the power-law fit. The uncertainty on electron temperature is not plotted, but instead is added in quadrature with the uncertainty to the flux density to give the uncertainty for the residual data points.